nature communications

Article

https://doi.org/10.1038/s41467-025-56902-x

Design of quinoline SARS-CoV-2 papain-like protease inhibitors as oral antiviral drug candidates

Received: 19 September 2024

Accepted: 29 January 2025

Published online: 13 February 2025

Check for updates

Prakash Jadhav[1,7], Xueying Liang[2,7], Ahmadullah Ansari[3,4,7], Bin Tan[1,7], Haozhou Tan[1], Kan Li[1], Xiang Chi[2], Alexandra Ford[5], Francesc Xavier Ruiz[3,4] ✉, Eddy Arnold[3,4] ✉, Xufang Deng[2,6] ✉ & Jun Wang[1] ✉

The ever-evolving SARS-CoV-2 variants necessitate the development of additional oral antivirals. This study presents the systematic design of quinoline-containing SARS-CoV-2 papain-like protease (PL^{pro}) inhibitors as potential oral antiviral drug candidates. By leveraging the recently discovered $Val70^{Ub}$ binding site in PL^{pro}, we designed a series of quinoline analogs demonstrating potent PL^{pro} inhibition and antiviral activity. Notably, the X-ray crystal structures of 6 lead compounds reveal that the 2-aryl substitution can occupy either the $Val70^{Ub}$ site as expected or the BL2 groove in a flipped orientation. The in vivo lead **Jun13296** exhibits favorable pharmacokinetic properties and potent inhibition against SARS-CoV-2 variants and nirmatrelvir-resistant mutants. In a mouse model of SARS-CoV-2 infection, oral treatment with **Jun13296** significantly improves survival, reduces body weight loss and lung viral titers, and prevents lung tissue damage. These results underscore the potential of quinoline PL^{pro} inhibitors as promising oral SARS-CoV-2 antiviral candidates, instilling hope for the future of SARS-CoV-2 treatment.

The COVID-19 pandemic has accelerated antiviral and vaccine development[1]. Drug repurposing was the primary strategy early in the pandemic, but genuinely new strategies have also emerged[2,3]. One of the ultimate goals is to develop broad-spectrum oral antivirals that can be used to prevent and treat pathogens with pandemic potential[4]. Priorities have been given to conserved viral targets, including polymerases and proteases. The SARS-CoV-2 RNA-dependent RNA polymerase (RdRp) inhibitors remdesivir and molnupiravir are known to have broad-spectrum antiviral activities against viruses in different families. For example, remdesivir, developed initially against the hepatitis C virus, has well-documented antiviral efficacy against filoviruses (e.g., Ebola, Marburg), coronaviruses (e.g., MERS-CoV, SARS-CoV, and SARS-CoV-2), *Pneumoviridae* (e.g., respiratory syncytial virus), and paramyxoviruses (e.g., Nipah, Hendra, measles, and mumps)[5,6]. Molnupiravir is effective against influenza viruses and coronaviruses[7]. Similarly, the SARS-CoV-2 main protease (M^{pro}) inhibitor nirmatrelvir has broad-spectrum antiviral activity against SARS-CoV, MERS-CoV, SARS-CoV-2, and common human coronaviruses HCoV-OC43, 229E, NL63, and HKU1[8,9]. Additional antivirals with alternative mechanisms of action are needed to combat viruses for which no antivirals are available or for which drug resistance issues with current antivirals are associated.

[1]Department of Medicinal Chemistry, Ernest Mario School of Pharmacy, Rutgers, the State University of New Jersey, Piscataway, NJ, USA. [2]Department of Physiological Sciences, College of Veterinary Medicine, Oklahoma State University, Stillwater, OK, USA. [3]Center for Advanced Biotechnology and Medicine, Rutgers, the State University of New Jersey, Piscataway, NJ, USA. [4]Department of Chemistry and Chemical Biology, Rutgers, the State University of New Jersey, Piscataway, NJ, USA. [5]Department of Veterinary Pathobiology, College of Veterinary Medicine, Oklahoma State University, Stillwater, OK, USA. [6]Oklahoma Center for Respiratory and Infectious Diseases, Oklahoma State University, Stillwater, OK, USA. [7]These authors contributed equally: Prakash Jadhav, Xueying Liang, Ahmadullah Ansari, Bin Tan. ✉e-mail: xavier@cabm.rutgers.edu; arnold@cabm.rutgers.edu; xufang.deng@okstate.edu; junwang@pharmacy.rutgers.edu

Structurally disparate compounds have been developed as SARS-CoV-2 M^{pro} inhibitors through high-throughput screening (HTS), fragment-based and structure-based design[1,10]. Paxlovid, a combination of the M^{pro} inhibitor nirmatrelvir and metabolic enhancer ritonavir, is approved by the FDA[9]. Ensitrelvir is a noncovalent M^{pro} inhibitor approved in Japan and Singapore[11]. Several additional M^{pro} inhibitors are at different stages of clinical trials, including Pfizer's second-generation inhibitor **PF-07817883** (Ibuzatrelvir)[12] and Merck's **MK-7845**[13]. Mutations have emerged in M^{pro} among circulating strains[14], including the predominant mutation P132H[15]. Fortunately, the P132H mutant remains sensitive to nirmatrelvir[15], and drug-resistant variants have yet to become prevalent in the clinic. Nevertheless, nirmatrelvir-resistant mutants have been identified from in vitro viral passage and enzymatic assay experiments[16–19]. The M^{pro} L50F/E166A/L167F triple mutant is of particular concern as the corresponding recombinant virus showed a high level of drug resistance while maintaining similar fitness of replication in cell culture and animals[19,20]. The Nsp5-L50F/E166V mutant was found in an immunocompromised human patient who underwent prolonged Paxlovid treatment[21].

The SARS-CoV-2 papain-like protease (PL^{pro}) is the second cysteine protease expressed by SARS-CoV-2 in addition to M^{pro} during viral replication. PL^{pro} is part of the non-structural protein 3 (nsp3) and cleaves viral polyproteins at the nsp1/2, nsp2/3, and nsp3/4 junctions[22]. PL^{pro} also has deubiquitinase and deISGylase activities and cleaves ubiquitin and ISG15 conjugates from host proteins, a mechanism to antagonize host immune responses[23,24]. Since the COVID-19 pandemic, the interest in developing PL^{pro} inhibitors has resurged, and several PL^{pro} inhibitors have been identified from HTS, drug repurposing, and virtual screening[25]. PL^{pro} is a cysteine protease with shallow S1 and S2 substrate binding sites (corresponds to Gly-Gly in substrates)[22], which accounts for the challenges in designing covalent and noncovalent PL^{pro} inhibitors[26]. The noncovalent naphthalene compound GRL0617 and its analogs are the major PL^{pro} inhibitors with a validated mechanism of action[25,27]. Our recent study revealed a first-in-class rationally designed noncovalent inhibitor **Jun12682** showing in vivo antiviral efficacy in a mouse model of SARS-CoV-2 infection[28]. **Jun12682** binds to the same site as GRL0617 in the blocking loop 2 (BL2) region. In addition, **Jun12682** extends to a previously unexplored binding site, $Val70^{Ub}$, which accounts for its high potency.

In this work, we design a series of quinoline analogs to similarly target the $Val70^{Ub}$ site. The X-ray crystal structures of PL^{pro} with six lead compounds reveal interesting findings: while five compounds, **Jun13317, Jun13306, Jun13307, Jun13308**, and **Jun13296** have their 2-aryl substituent occupying the $Val70^{Ub}$ site as expected, **Jun12665** adopts a flipped orientation with the 2-pyrazolyl substitution fitting in the BL2 groove site. The in vivo lead **Jun13296** displays more potent enzymatic inhibition and antiviral activity than the previously reported biarylphenyl inhibitor **Jun12682**. In a SARS-CoV-2 infection mouse model, oral treatment of **Jun13296** displays improved in vivo antiviral efficacy than **Jun12682**. Collectively, **Jun13296** represents a promising PL^{pro} antiviral drug candidate for further development.

Results

Design of quinoline SARS-CoV-2 PL^{pro} inhibitors

We recently designed a covalent inhibitor, **Jun11313**, showing potent enzymatic inhibition with an IC_{50} of 0.12 μM[28]. The X-ray crystal structure of PL^{pro}-**Jun11313** (PDB: 8UVM) uncovered a previously unexplored drug binding site, $Val70^{Ub}$, which accommodates the Val70 and Leu71 side chains from ubiquitin as well as the thienyl substituent in **Jun11313** (Fig. 1a). Superposition of the X-ray crystal structures of

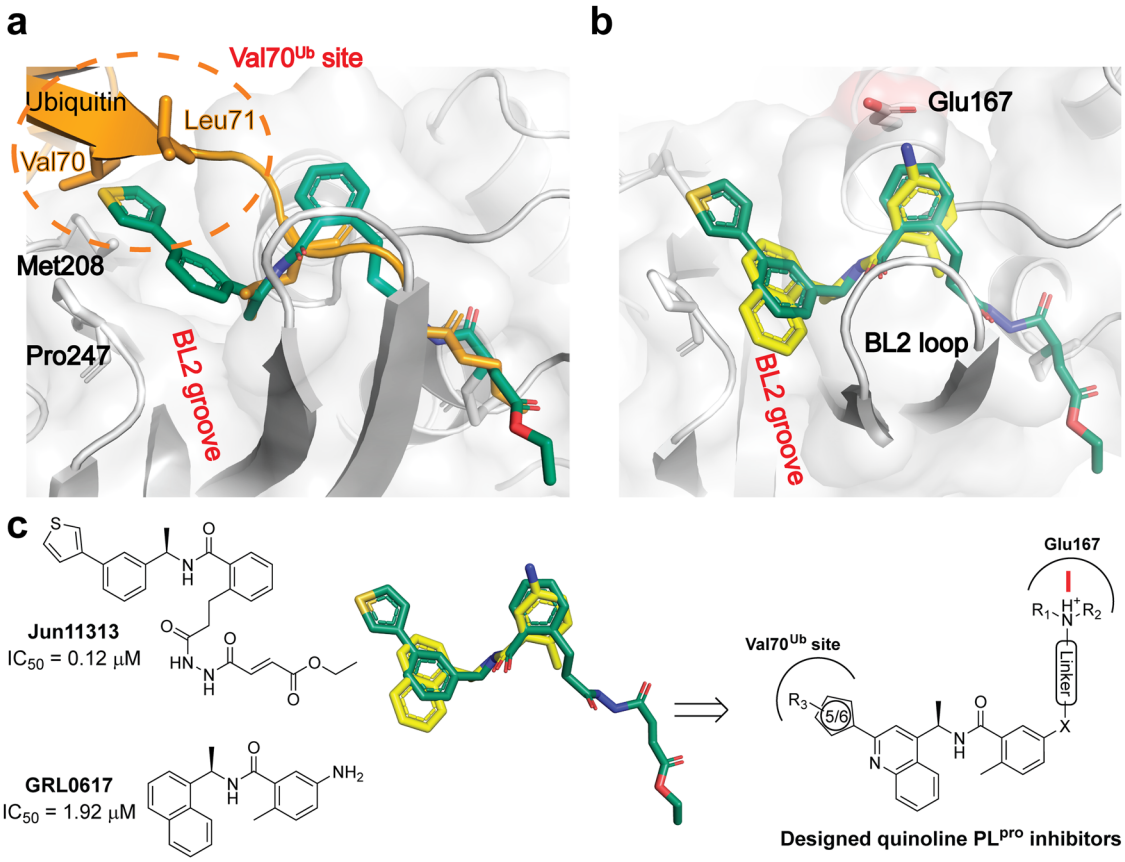

Fig. 1 | Design of quinoline SARS-CoV-2 PL^{pro} inhibitors. a Superposition of the X-ray crystal structures of SARS-CoV-2 PL^{pro} with **Jun11313** (green) (PDB: 8UVM) and ubiquitin (orange) (PDB: 6XAA). **b** Superposition of the X-ray crystal structures of SARS-CoV-2 PL^{pro} with **Jun11313** (green) (PDB: 8UVM) and GRL0617 (yellow) (PDB: 7JRN). **c** Design of the quinoline PL^{pro} inhibitors based on **Jun11313** and GRL0617. Source data of (**c**) are provided as a Source Data file.

SARS-CoV-2 PL^{pro} with **Jun11313** (green) (PDB: 8UVM) and GRL0617 (yellow) (PDB: 7JRN) (Fig. 1b) suggests that the benzene ring in **Jun11313** can be expanded to naphthalene to engage additional hydrophobic interactions with residues in the BL2 loop region (Fig. 1c). For the convenience of installing various aromatic substitutions to target the $Val70^{Ub}$ binding site, we replaced the naphthalene ring with quinoline in our inhibitor design (Fig. 1c). In addition, a terminal positively charged amino group is added at the meta-position of the benzoic acid through a linker to bridge the electrostatic interaction with Glu167. Previous studies have shown that this design strategy improves the binding affinity of PL^{pro} inhibitors[28,29]. The position of the linker attachment and the types of linkers chosen for the design were informed by previous structure-activity relationship results and the molecular docking results of the virtual library of designed compounds[28–30].

Guided by the design hypothesis illustrated in Fig. 1c, we initiated a stepwise lead optimization on the quinoline PL^{pro} inhibitors (Fig. 2, Supplementary Fig. 1). We first fixed the amine substituent and explored 2-aryl substitutions in the quinoline (Supplementary Fig. 1a), followed by varying the amine substituents (Supplementary Fig. 1b, c). A virtual library sharing the common scaffold, as shown in Fig. 1c, was created and docked in PL^{pro} using Schrödinger Glide's extra precision. Prioritized hits were then synthesized and tested in the Förster resonance energy transfer (FRET) enzymatic assay using the FRET substrate containing the viral polyprotein nsp2/3 cleavage sequence and cytotoxicity assay in Vero E6 cells. Promising leads were tested in the PL^{pro} FlipGFP assay, a cell-based PL^{pro}-specific protease assay that correlates well with antiviral activity[31,32]. Next, the leads were tested in the SARS-CoV-2 antiviral assay in the Caco-2-ACE2-TMPRSS2 cell line and profiled for mouse liver microsomal stability ($T_{1/2}$). Representative potent lead compounds are shown in Fig. 2. The biarylphenyl PL^{pro} inhibitor **Jun12682** was included as a positive control (Fig. 2a)[28]. Thienyl, furanyl, thiazole, pyrazole, and pyridine substituents were all tolerated at the 2-aryl position (Supplementary Fig. 1a), suggesting the $Val70^{Ub}$ site can accommodate a diverse set of aromatic substituents through hydrophobic interactions. This result is consistent with the previous structure-activity relationship (SAR) result of the biarylphenyl series of inhibitors[28]. Compounds with pyrazole substituents, including **Jun12315, Jun1285, Jun12226**, and **Jun1275**, had potent enzymatic inhibition (IC_{50} = 0.19–0.25 μM) and low cytotoxicity (CC_{50} = 63.1–146.3 μM). **Jun12665** had potent enzymatic inhibition (IC_{50} = 0.14 μM, K_i = 32.1 nM), but displayed weak cellular activity in the FlipGFP assay (EC_{50} = 32 μM), possibly due to poor membrane permeability. Next, we examined different amine substitutions (Supplementary Fig. 1b, c). Nine lead compounds had potent enzymatic inhibition, including the pyrrolidine analogs **Jun13306** (IC_{50} = 0.18 μM, K_i = 25.8 nM) and **Jun13307** (IC_{50} = 0.16 μM, K_i = 25.4 nM), the azetidine analogs **Jun1393** (IC_{50} = 0.28 μM, K_i = 45.0 nM) and **Jun13338** (IC_{50} = 0.17 μM, K_i = 39.6 nM), the piperazine analogs **Jun13126** (IC_{50} = 0.27 μM, K_i = 64.8 nM), **Jun13317** (IC_{50} = 0.20 μM, K_i = 47.4 nM), and **Jun13308** (IC_{50} = 0.14 μM, K_i = 19.3 nM), the 3,8-diazabicyclo[3.2.1] octane analog **Jun13296** (IC_{50} = 0.13 μM, K_i = 8.8 nM), and the

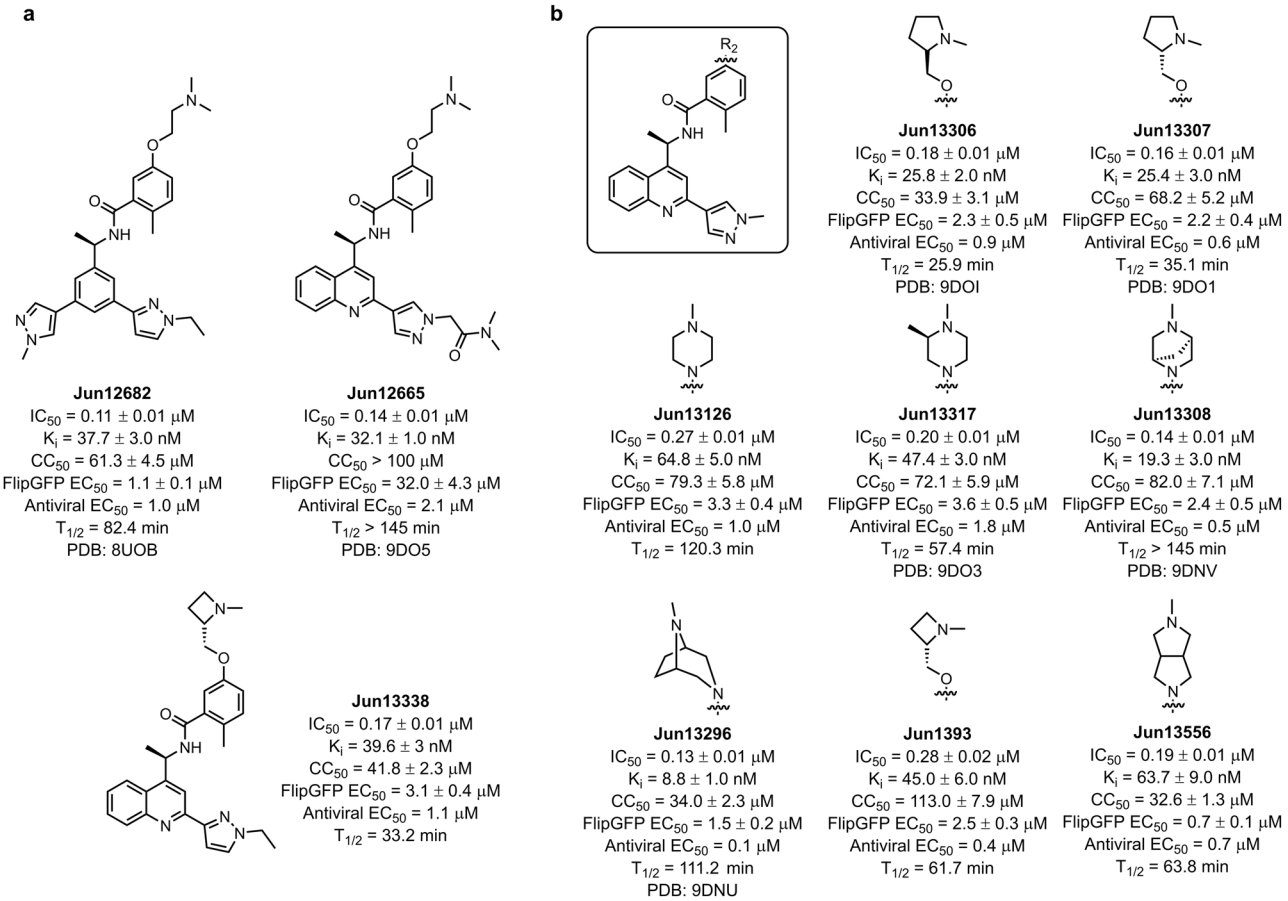

Fig. 2 | Representative quinoline SARS-CoV-2 PL^{pro} inhibitors. a Chemical structure and in vitro activities of **Jun12682, Jun12665**, and **Jun13338. b** Chemical structures and in vitro activities of quinoline analogs with diverse amine substituents. IC_{50}, half maximal inhibitory concentration in the FRET enzymatic assay; K_i, inhibitory constant in the FRET enzymatic assay; CC_{50}: half maximal toxicity concentration in Vero cells, CC_{50} values are mean ± S.D. of three technical repeats; EC_{50}, half maximal effective concentration in the FlipGFP and antiviral assays, EC_{50} values are mean ± standard deviation of three technical repeats; $T_{1/2}$, half-life in mouse liver microsomal stability assay. Source data are provided as a source data file.

octahydropyrrolo[3,4-c]pyrrole analog **Jun13556** (IC_{50} = 0.19 μM, K_i = 63.7 nM) (Fig. 2). The positive control **Jun12682** had an antiviral EC_{50} of 1.0 μM. Seven compounds showed comparable or enhanced antiviral potency, including **Jun13306** (EC_{50} = 0.9 μM), **Jun13307** (EC_{50} = 0.6 μM), **Jun13126** (EC_{50} = 1.0 μM), **Jun13308** (EC_{50} = 0.5 μM), **Jun13296** (EC_{50} = 0.1 μM), **Jun1393** (EC_{50} = 0.4 μM), and **Jun13556** (EC_{50} = 0.7 μM). Among the list of analogs, **Jun13296** is the most active lead compound with an antiviral EC_{50} value of 0.1 μM, a 10-fold improvement compared to **Jun12682** (EC_{50} = 1.0 μM). The potent antiviral activity of **Jun13296** correlates with its high enzymatic inhibitory activity (IC_{50} = 0.13 μM, K_i = 8.8 nM) and cellular PL^{pro} inhibitory activity in the Flip-GFP assay (EC_{50} = 1.5 μM). Selective compounds were profiled for mouse liver microsomal stability to prioritize lead candidates for the in vivo PK and antiviral efficacy studies. **Jun12665, Jun13126, Jun13308**, and **Jun13296** showed the highest microsomal stability ($T_{1/2}$ > 100 min).

In vivo pharmacokinetic (PK) properties of quinoline SARS-CoV-2 PL^{pro} inhibitors

Eight compounds were selected for in vivo oral snapshot PK studies in mice based on their antiviral activity and mouse liver microsomal stability (Fig. 2, Supplementary Fig. 1). Compounds were formulated in 0.5% methylcellulose and 2% Tween 80 in water and dosed in 3 male C57BL/6J mice through oral gavage. Blood samples were collected from the tail vein at 0.5, 1, 3, and 5 h to quantify plasma drug concentrations by LC-MS/MS. **Jun13306, Jun13317, Jun13338**, and **Jun13126** had fast absorption and reached the maximum plasma concentrations at the first time point of 0.5 h (Fig. 3a, b). In contrast, **Jun13308** and **Jun13296** absorbed relatively slower and reached the maximum plasma concentrations at 3 h. **Jun13296** displayed the highest drug concentrations at 3 h (3530 ng/mL) and 5 h (3040 ng/mL) and was thus selected for a 24 h in vivo PK study to determine the oral bioavailability. Interestingly, both the intravenous (i.v.) and *per os* (p.o., oral) administrations of **Jun13296** showed a biphasic drug exposure pattern (Fig. 3c). Following p.o. administration at 50 mg/kg, **Jun13296** reached the peak plasma concentration (C_{max}) of 6,957 ng/mL at 2 h, followed by a decline to 664 ng/mL at 4 h, and an increase to 2413 ng/mL at 8 h. Similarly, for the i.v. administration at 10 mg/kg, the drug concentrations decreased from 3553 ng/mL at 0.25 h to 1527 ng/mL at 2 h, followed by an increase to 5637 ng/mL at 4 h. The half-lives ($T_{1/2}$) were 2.4 h and 3.4 h for i.v. and p.o. administrations (Fig. 3d). The oral bioavailability of **Jun13296** was 32.8%. The plasma concentration of **Jun13296** was maintained above the antiviral EC_{90} values for over 8 h with oral dosing at 50 mg/kg (Fig. 3c).

Jun13296 was selected for further in vitro PK profiling. **Jun13296** is stable in mouse and human liver microsomal stability assays with $T_{1/2}$ of 111.2 and 73.6 min, respectively. **Jun13296** did not inhibit five representative CYP isoforms 1A2, 2C9, 2C19, 2D6, and 3A-M (IC_{50} > 50 μM) (Fig. 3e), indicating it might not have the drug-drug interaction issue associated with the M^{pro} inhibitor nirmatrelvir. The mouse plasma protein binding for **Jun13296** is 94.1%. The high plasma protein binding ratio of **Jun13296** might account for its in vivo biphasic drug exposure. **Jun13296** has moderate permeability in Egg- Parallel Artificial Membrane Permeability Assay (PAMPA) and blood-brain barrier specific (BBB)-PAMPA assays with P_e values of 11.0 and 10.9 nm/s. Overall, **Jun13296** has favorable in vitro and in vivo PK properties that warranted advancing to the in vivo antiviral efficacy study in mice.

Mechanism of action of Jun13296

Jun13296 displayed dose-dependent stabilization of SARS-CoV-2 PL^{pro} in the differential scanning fluorimetry assay (Fig. 4a), with a larger stabilization (and hence higher binding affinity) than **Jun12682**, consistent with the enzymatic FRET protease assay results (Fig. 1). To characterize whether **Jun13296** inhibits the deubiquitinase and

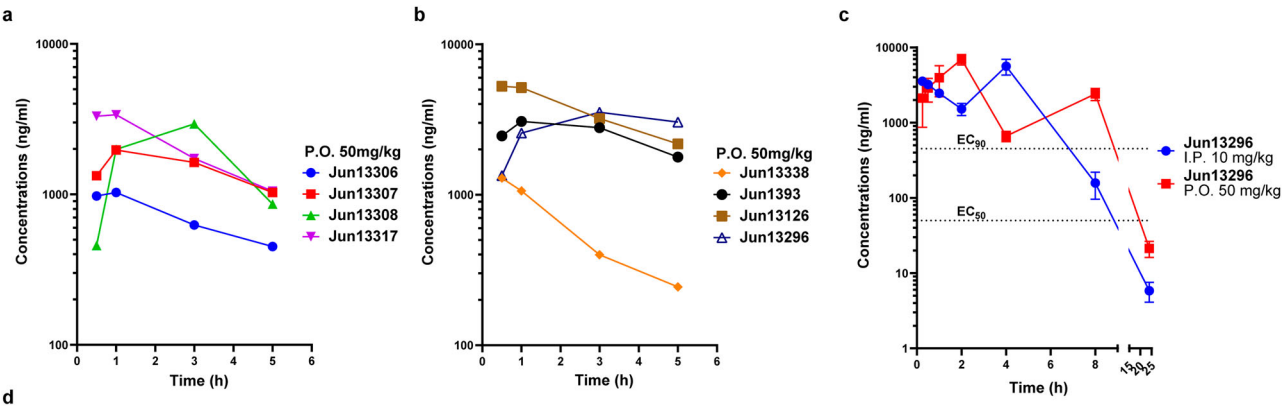

d

Compound	$T_{1/2}$ (h)	T_{max} (h)	C_{max} (ng/mL)	AUC_{0-t} (h•ng/mL)	$AUC_{t-\infty}$ (h•ng/mL)	CL (mL/min/kg)	$MRT_{t-\infty}$ (h)	V_{ss} (mL/kg)	F (%)
Jun13296 (i.v.)	2.4 ± 0.3			25206 ± 4875	25227 ± 4868	6.76 ± 1.19	3.52 ± 0.14	1.42 ± 0.20	
Jun13296 (p.o.)	3.4 ± 0.3	2.0 ± 0.0	6957 ± 1099	41318 ± 3916	41423 ± 3932		5.61 ± 0.46		32.8 ± 3.1

e

Compound	Mouse liver microsomal stability	Human liver microsomal stability	CYP inhibition	Mouse plasma protein binding	Egg-PAMPA	BBB-PAMPA
Jun13296	$T_{1/2}$ = 111.2 min $C_{Lint(mic)}$ = 12.5 μL/min/mg $CL_{int(liver)}$ = 49.4 mL/min/kg	$T_{1/2}$ = 73.6 min $C_{Lint(mic)}$ = 18.8 μL/min/mg $CL_{int(liver)}$ = 16.9 mL/min/kg	CYP1A2: IC_{50} > 50 μM CYP2C9: IC_{50} > 50 μM CYP2C19: IC_{50} > 50 μM CYP2D6: IC_{50} > 50 μM CYP3A-M: IC_{50} > 50 μM	94.1%	11.0 nm/s	10.9 nm/s

Fig. 3 | In vitro and In vivo PK SARS-CoV-2 PL^{pro} inhibitors. a Plasma drug concentration of **Jun13306, Jun13307, Jun13308**, and **Jun13317** in C57BL/6J mice (6 to 8 weeks old) following p.o. administration of 50 mg/kg of compounds in 0.5% methylcellulose and 2% Tween 80 in water (n = 3 per group). **b** Plasma drug concentrations of **Jun13338, Jun1393, Jun13126**, and **Jun13296** in C57BL/6J mice (6 to 8 weeks old) following p.o. administration of 50 mg/kg of compounds in 0.5% methylcellulose and 2% Tween 80 in water (n = 3 per group). **c** Plasma drug concentrations of **Jun13296** in C57BL/6J mice (6 to 8 weeks old) following p.o. administration of 50 mg/kg and i.v. injection of 10 mg/kg (n = 3 per group) of compound. The error bars are mean ± s.d. **d** In vivo pharmacokinetic parameters of **Jun13296** in C57BL/6J mice. **e** In vitro pharmacokinetic parameters of **Jun13296**. $T_{1/2}$, half-life; T_{max}, time for maximal concentration; C_{max}, maximum plasma concentration; AUC_{0-t}, area under the curve from time zero to time t; $AUC_{t-\infty}$, area under the curve from time t to infinity; CL, clearance; MRT, mean residence time; V_{ss}, volume of distribution; F, oral bioavailability. Source data are provided as a source data file.

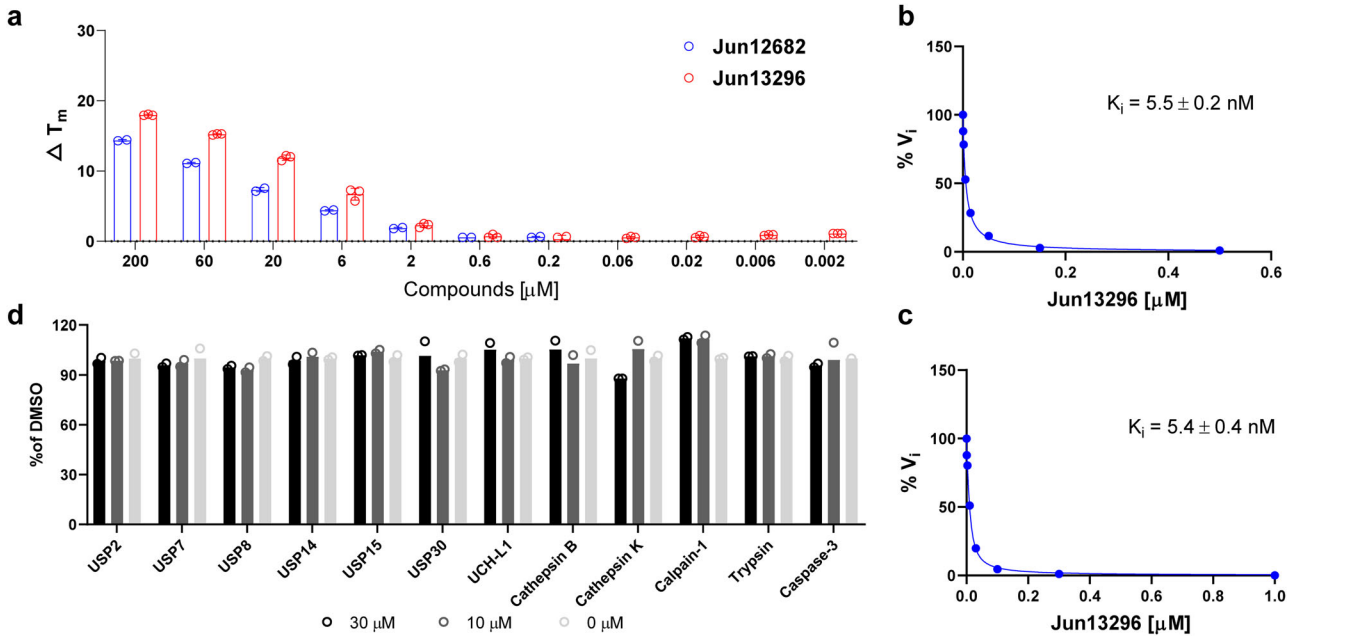

Fig. 4 | Mechanistic studies of Jun13296. a Differential scanning fluorimetry assay of **Jun13296** in stabilizing SARS-CoV-2 PL^{pro}. **Jun12682** was included as a positive control for comparison. Data from **Jun12682** is the mean of two repeats, and data from **Jun13296** is the mean ± standard deviation of three technical repeats. **b** K_i plot of **Jun13296** in inhibiting SARS-CoV-2 PL^{pro} hydrolysis of ISG15-AMC. **c** K_i plot of **Jun13296** in inhibiting SARS-CoV-2 PL^{pro} hydrolysis of Ub-AMC. **d** Counter screening of Jun**13296** against host proteases USP2, USP7, USP8, USP14, USP15, USP30, UCH-L1, cathepsin B, cathepsin K, calpain-1, trypsin, and caspase 3. Data in (**d**) are presented as mean ± standard deviation of two technical repeats. Source data are provided as a source data file.

deISGylase activities of SARS-CoV-2 PL^{pro}, we tested **Jun13296** in the PL^{pro} enzymatic assays using ubiquitin-AMC (7-amino-4-methylcoumarin) and ISG15-AMC substrates, respectively. **Jun13296** inhibited the deubiquitinase and deISGylase activities of PL^{pro} with K_i values of 5.5 nM and 5.4 nM (Fig. 4b, c), similar to its activity in inhibiting the hydrolysis of the viral polyprotein nsp2/3 substrate (K_i = 8.8 nM) (Fig. 2). To profile the selectivity of **Jun13296**, we tested it against a panel of host proteases, including human deubiquitinases USP2, USP7, USP8, USP14, USP15, USP30, UCH-L1, cathepsin B, cathepsin K, calpain-1, trypsin, and caspase 3[29,33]. **Jun13296** did not inhibit these host proteases at up to 30 μM (Fig. 4d), suggesting **Jun13296** is specific for the viral PL^{pro}. Other PL^{pro} inhibitors, including GRL0617 analogs and **PF-07957472**, similarly showed a high selectivity over host proteases as reported[33,34].

X-ray crystal structures of SARS-CoV-2 PL^{pro} with quinoline inhibitors

The inhibitor-bound X-ray co-crystal structures of SARS-CoV-2 wild-type PL^{pro} were determined for six noncovalent quinoline series compounds: **Jun12665, Jun13317, Jun13306, Jun13307, Jun13308**, and **Jun13296**, with resolutions ranging from 2.30 Å to 2.95 Å (Supplementary Table 1). The electron density maps clearly delineate the protein molecule, coordinated zinc, and inhibitors (Supplementary Fig. 2), confirming their orientations and interactions with the surrounding environment (Fig. 5a–f). All inhibitors consistently bind at the same site, interacting with the BL2 loop, the Glu167 side chain, and the recently identified $Val70^{Ub}$ site within the extended peptide binding region of PL^{pro}, distal from the active site triad (Cys111, His272, and Asp286) (Fig. 5a–f and Supplementary Fig. 2a, b). This binding follows a conserved interaction pattern involving Asp164, Glu167, Pro247, Pro248, Tyr264, Tyr268, and Gln269 of wild-type PL^{pro}. All inhibitors' 2-aryl substituted quinoline aromatic rings, except **Jun12665**, orient toward the $Val70^{Ub}$ site, consistent with our design hypothesis (Fig. 1b). The quinoline moiety of the inhibitors is stabilized by hydrophobic interactions and π-stacking interactions with Tyr268, Tyr264, Pro248, and Pro247, as well as CH–π and S–π interactions with Met208, as previously reported[28]. **Jun12665**, with its amide pyrazole substitution, occupies the previously reported BL2 groove site and forms hydrophobic interactions with Pro247, Pro248, Tyr264, and Tyr268 (Fig. 5a). The terminal dimethylamide carbonyl oxygen forms an additional hydrogen bond with the main-chain amide nitrogen of Tyr268 (Fig. 5a, Supplementary Fig. 2a), which might account for the flipped orientation of **Jun12665** compared with the other inhibitors (Fig. 5g). The central amide linker regions of all six inhibitors are stabilized through hydrogen bonds with the carboxylate side chain of Asp164 and the main-chain amide nitrogen of Tyr268. Various substituents at the positions of previously published dimethylamino moieties engage in electrostatic interactions with the Glu167 carboxylate across all structures, showing slight variations in bonding distances and the number of Glu167 oxygen atoms involved in the interactions (Fig. 5). **Jun13306** and **Jun13307** containing the R and S pyrrolidine substitutions both form similar electrostatic interactions with the Glu167 carboxylate (Fig. 5b, c, h, Supplementary Fig. 2g), corroborating their equivalent enzymatic inhibitory activities (K_i = 25.8 and 25.4 nM) (Fig. 2).

The superimposed X-ray crystal structure of PL^{pro}/**Jun13296** with host deubiquitinases, USP2, USP7, and USP14, showed that the $Val70^{Ub}$ and BL2 groove binding sites are absent in these host deubiquitinases (Supplementary Fig. 3), which accounts for the high selectivity of **Jun13296**.

In vitro and in vivo antiviral activities of Jun13296

Given the distinct mechanism of action of PL^{pro} inhibitors from M^{pro} inhibitor nirmatrelvir and the sequence conservation of PL^{pro}, **Jun13296** is expected to have broad-spectrum antiviral activity against nirmatrelvir-resistant mutants and SARS-CoV-2 variants. For this, we tested **Jun13296** against the nirmatrelvir-resistant SARS-CoV-2 viruses rNsp5-L50F/E166V and rNsp5-L50F/E166A/L167F, and the recently circulating SARS-CoV-2 omicron variants XBB.1.16 and JN.1 in plaque assay (Fig. 6, Supplementary Fig. 4). Nsp5-L50F/E166V mutant was identified from an immunocompromised human patient with prolonged Paxlovid treatment[21]. Nsp5-L50F/E166A/L167F mutant was

https://doi.org/10.1038/s41467-025-56902-x

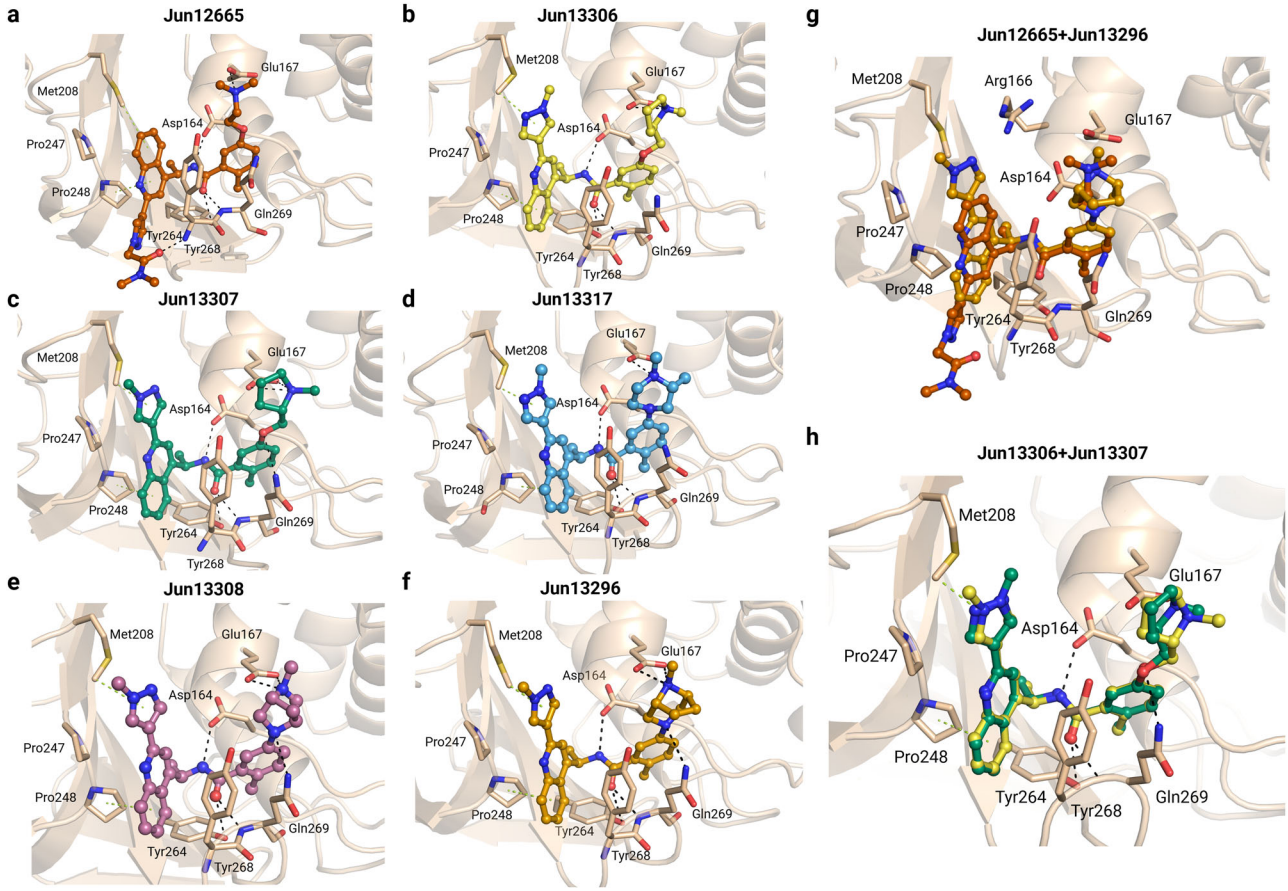

Fig. 5 | X-ray crystal structures of SARS-CoV-2 PL^{pro} with quinoline inhibitors. Binding of quinoline inhibitors to SARS-CoV-2 PL^{pro}. **a**–**f** Interactions of **Jun12665** (orange), **Jun13306** (yellow), **Jun13307** (green), **Jun13317** (light blue), **Jun13308** (magenta), and **Jun13296** (bright orange) with PL^{pro} are conserved (residues within 5 Å of the inhibitor are shown as light brown sticks). Hydrogen bonds are indicated by black dashed lines, van der Waals contacts by red dashed lines, and π–π interactions by light green dashed lines. **g** The superposition of **Jun12665** onto **Jun13296** represents the flipped orientation of terminal amide carbonyl groups toward the BL2 groove. **h** Superposition of **Jun13306** (yellow) and **Jun13307** (green) containing the R and S pyrrolidine substituents both form similar electrostatic interactions with the Glu167 carboxylate.

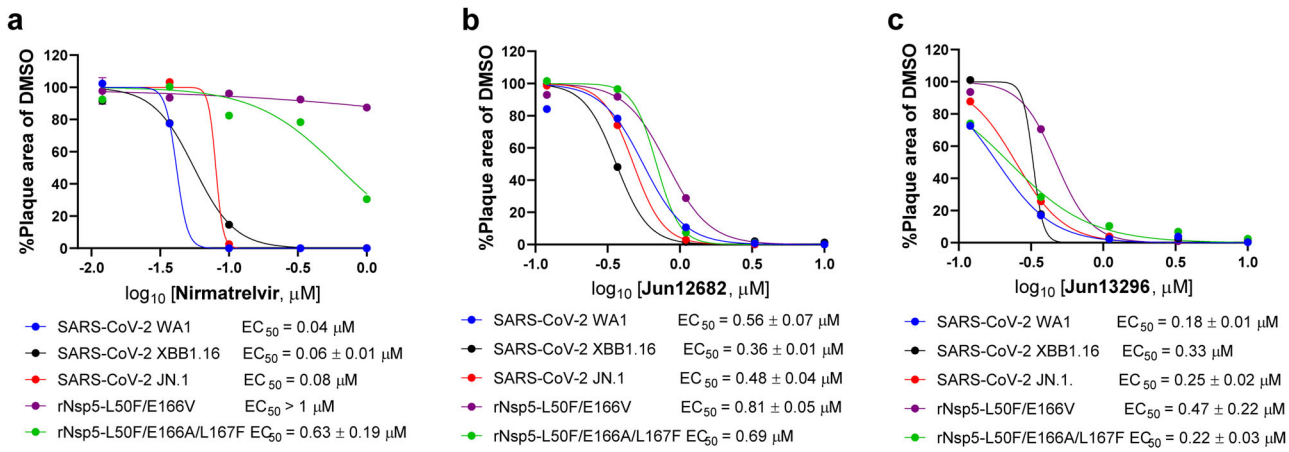

Fig. 6 | Broad-spectrum antiviral activity of SARS-CoV-2 PL^{pro} inhibitors. The antiviral activity of nirmatrelvir, **Jun12682**, and **Jun13296** was tested in the plaque assay using Vero-ACE2-TMPRSS2 (Vero-AT) cells. **a** Plaque assay EC_{50} plots of nirmatrelvir. **b** Plaque assay EC_{50} plots for **Jun12682**. **c** Plaque assay EC_{50} plots of Jun13296. EC_{50} values are mean ± standard deviation of two technical repeats. Source data are provided as a source data file.

selected under drug selection pressure in the cell culture viral passage experiment[18,19]. The M^{pro} inhibitor nirmatrelvir and the previously reported PL^{pro} inhibitor **Jun12682** were included as controls. All three inhibitors showed potent inhibition against SARS-CoV-2 WA1 and the omicron variants XBB1.16 and JN.1 (Fig. 6a–c). The rNsp5-L50F/E166V and rNsp5-L50F/E166A/L167F viruses had significant resistance against nirmatrelvir with EC_{50} values of >1 μM, and 0.63 μM, respectively (Fig. 6a). In contrast, **Jun13296** displayed consistent antiviral potency against the rNsp5-L50F/E166V and rNsp5-L50F/E166A/L167F mutants with EC_{50} values of 0.47 and 0.22 μM, respectively (Fig. 6c), and was

https://doi.org/10.1038/s41467-025-56902-x

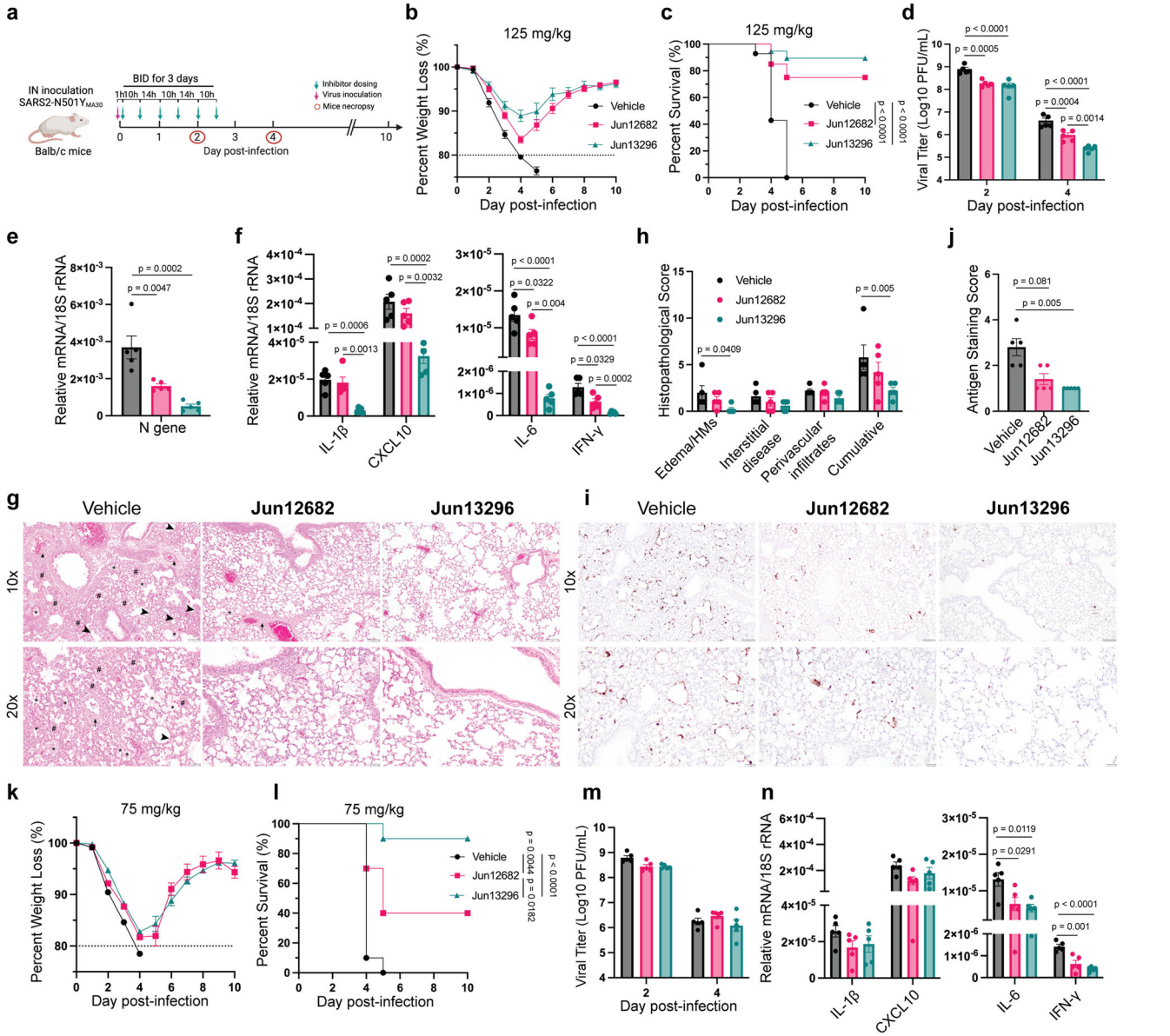

Fig. 7 | In vivo antiviral efficacy of Jun13296. a Experimental design for twice-a-day (BID) treatment for 3 days. **b** Mouse body weight loss and **c** survival rate of the mice receiving a 125 mg/kg BID_3 treatment. Data in (**b**, **c**) are pooled results of four independent experiments and are shown as mean ± standard error of the mean (SEM) ($n = 14$, 20, 19 mice for the Vehicle, **Jun12682**, and **Jun13296** group, respectively). **d** Viral titers in lungs ($n = 5$ per group). Quantitative PCR analysis of viral nucleocapsid gene (**e**) and cellular cytokines (**f**) in lungs ($n = 5$ per group). **g** Haematoxylin and eosin (H&E) staining of lungs collected 4 DPI ($n = 5$ per group). Lungs exhibited airway edema (asterisks), hyaline membranes (HM, arrowheads), perivascular cuffing (arrows), and interstitial thickness (number sign). Scale bars, 100 mm (top) and 50 mm (bottom). **h** Quantification of the pathological lesions (**g**). **i** Immunostaining of lungs collected 4 DPI ($n = 5$ per group) for SARS-CoV-2 nucleocapsid protein (brown color staining). Scale bars, 100 μm (top) and 50 μm (bottom). **j** Summary scores of nucleocapsid immunostaining of lungs. **k** Mouse body weight loss and **l** survival rate of the mice receiving a 75 mg/kg BID_3 treatment. Data are pooled results of two independent experiments ($n = 10$ per group) and are shown as mean ± SEM. **m** Viral titers in lungs ($n = 5$ per group). **n** Quantitative PCR analysis of cellular cytokines in lungs collected 2 DPI ($n = 5$ per group). Data in (**c**, **l**) are shown as mean ± SEM, and the p values were determined using a log-rank (Mantel-Cox) test. Data in (**d**, **m**) are shown as mean ± SEM and analyzed with a two-way ANOVA Tukey's multiple comparison test. Data in (**e**, **f**, **n**) are shown as mean ± SEM and analyzed with a one-way ANOVA multiple comparison test for each tested gene. Data in (**h**, **j**) are mean ± SEM and analyzed with the Krushal-Wallis multiple comparisons test for each category. Source data are provided as a source data file. **a** was created with Biorender.com. Li, K. (2025) https://BioRender.com/q16l908.

more potent than **Jun12682** (Fig. 6b). Collectively, these results show that PL^{pro} inhibitors have consistent antiviral activity against SARS-CoV-2 variants and nirmatrelvir-resistant strains.

To evaluate the in vivo antiviral efficacy of **Jun13296**, we utilized a lethal SARS-CoV-2 mouse model that has been widely accepted for assessing SARS-CoV-2 therapeutics and vaccine candidates[35–38]. We previously reported the antiviral efficacy of **Jun12682** using this model[28]. Hence, **Jun12682** was included as a control in this study. To this end, young female BALB/c mice were intranasally inoculated with 6,000 PFU of SARS2-N501Y$_{MA30}$ and orally administered PL^{pro} inhibitors or vehicle one hour after virus inoculation, followed by twice daily dosing with a 10- and 14-h interval within 24 h for 3 consecutive days (Fig. 7a). A subgroup of 5 mice from each treatment group were necropsied at 2- and 4-day post-infection (DPI) to collect lung tissues for viral load and histopathological assessment. We first evaluated the antiviral efficacy of a 125 mg/kg dose. The weight loss plot (Fig. 7b) illustrates that vehicle-treated mice experienced rapid body weight loss exceeding 20% by 4 DPI. In contrast, both **Jun12682**- and

Jun13296-treated mice exhibited reduced weight loss and had maximal weight loss at 4 DPI, following body weight regain. Specifically, **Jun13296**-treated mice had an average of 11% maximal weight loss, significantly less than the maximal weight loss of **Jun12682**-treated mice (17%, $p < 0.001$) and the vehicle group (21%, $p < 0.0001$). Survival analyses demonstrated that inhibitor-treated groups had statistically higher survival rates compared to the vehicle group (0% survival rate): **Jun13296** (90%, $p < 0.0001$), and **Jun12682** (75%, $p < 0.0001$) (Fig. 7c). We previously demonstrated a 125 mg/kg dosage of **Jun12682**, administered with an 8-hour and 16-hour interval between doses within 24 h, provided only 20% protection[28]. Our current results indicate that administrating doses with 10-h and 14-h intervals offers improved protection, likely due to maintaining effective plasma concentrations as suggested by the in vivo PK data[28]. Viral load analyses of mouse lungs revealed that the vehicle-treated mice had robust infections in the lungs at 2 DPI with a mean titer of $\log_{10}$ 8.87 ± 0.079 PFU/mL. In contrast, the **Jun12682**- and **Jun13296**-treated mice had statistically lower lung viral titers, $\log_{10}$ 8.25 ± 0.064 PFU/mL ($p = 0.0005$), and $\log_{10}$ 8.11 ± 0.137 PFU/mL ($p < 0.0001$), respectively (Fig. 7d). The titer reductions were more evident at 4 DPI with a half-log lower titer ($\log_{10}$ 5.94 ± 0.115 PFU/mL, $p = 0.0004$) for the **Jun12682**-treated mice and over a log titer reduction ($\log_{10}$ 5.38 ± 0.059 PFU/mL, $p < 0.0001$) for the **Jun13296**-treated mice compared to the mean titer ($\log_{10}$ 6.57 ± 0.115 PFU/mL) of the vehicle group (Fig. 7d). The 4 DPI titer of the **Jun13296** group is significantly lower than that of the **Jun12682** group ($p = 0.0014$). These results corroborate the weight loss and survival data (Fig. 7b, c).

Quantitative PCR analysis of the RNA samples extracted from 2 DPI mice lungs showed that the 125 mg/kg dosage of either PL^{pro} inhibitor significantly reduced the expression of the viral nucleocapsid (N) gene (Fig. 7e) and multiple inflammatory cytokines, including *IL-1β*, *CXCL10*, *IL-6*, and *IFN-γ* (Fig. 7f). The relative mRNA levels of these cytokines in the lungs of **Jun13296**-treated mice are significantly lower than those of **Jun12682**-treated mice. Histopathological analysis of mouse lungs collected at 4 DPI reveals that the vehicle-treated, SARS2-$N501Y_{MA30}$-infected mice exhibited multifocal pulmonary lesions, including lymphocytic perivascular cuffing, pulmonary edema, hyaline membrane formation, and interstitial thickening and inflammation (Fig. 7g). In contrast, the mice that received 125 mg/kg BID of PL^{pro} inhibitors exhibited overall reduced lung histopathological manifestations with statistically significant improvement in the **Jun13296**-treatment group (Fig. 7h). Immunohistochemical (IHC) analysis of mouse lungs using a monoclonal antibody to detect SARS-CoV-2 N protein demonstrated strong and expansive antigen staining in lungs from vehicle-treated, infected mice, whereas inhibitor-treated considerably decreased viral antigen staining levels with a few sporadic positive cells (Fig. 7i). Lungs of **Jun13296**-treated mice had significantly less antigen staining than the lungs of the vehicle group (Fig. 7j), consistent with the lung viral titer results (Fig. 7d). The reduced viral replication in the lung and the expression of inflammatory cytokines (Fig. 7d–f) corroborate with the reduced lung inflammation and N protein staining at 4 DPI (Fig. 7g–j).

We further evaluated a lower dosage of 75 mg/kg. During this treatment, despite the mice administered with either inhibitor experiencing more maximal weight loss than the mice receiving the 125 mg/kg dosage (Fig. 7k), the **Jun13296** treatment rendered 90% protection, significantly higher than vehicle treatment ($p < 0.0001$) (Fig. 7l). **Jun12682** treatment instead provided only 40% protection, higher than the vehicle group ($p = 0.0044$) but significantly lower than the **Jun13296** treatment ($p = 0.0182$) (Fig. 7l). Viral load analysis of mouse lungs revealed statistically insignificant titer reductions at 2 and 4 DPI (Fig. 7m). Quantitative PCR analysis of the RNA samples extracted from 2 DPI mice lungs showed that the 75 mg/kg dosage of either inhibitor significantly reduced the expression of *IL-6* and *IFN-γ* but not *IL-1β* and *CXCL10* (Fig. 7n). These results suggest that a 75 mg/kg dosage of **Jun13296** or **Jun12682** still provides evident protection without markedly lowering viral loads in the lung. *IL-6* is a biomarker associated with adverse clinical outcomes in SARS-CoV-2 infection, and blockade of *IL-6* signaling has been shown to improve outcomes in critically ill COVID-19 patients[39–44]. A high level of *IFN-γ* was observed in severe COVID-19 cases and was associated with lung fibrosis[45–48]. Significantly reduced expression of IL-6 and *IFN-γ* in the inhibitor-treated groups may contribute to improved mouse survival (Fig. 7k, l).

Discussion

Compared to the successful development of SARS-CoV-2 M^{pro} inhibitors, PL^{pro} has proven to be a challenging antiviral drug target[25]. Designing PL^{pro} inhibitors with in vivo antiviral efficacy has only become a reality very recently[28,34]. With the potential threat of drug-resistant mutants against M^{pro} and RdRp inhibitors, there is a dire need for additional antivirals with alternative mechanisms of action. Given its sequence conservation and multi-faceted roles in viral replication, PL^{pro} has been enlisted as a high-profile antiviral drug target[25]. We recently reported the design of a biarylphenyl inhibitor **Jun12682** showing in vivo antiviral efficacy in a SARS-CoV-2 infection mouse model[28]. The high antiviral potency of **Jun12682** stems from its dual targeting mode by binding to the $Val70^{Ub}$ site and the previously reported BL2 groove[28]. Given the high triage rate in translational development, additional PL^{pro} inhibitors with novel scaffolds are needed as backups. In this study, we designed quinoline-containing PL^{pro} inhibitors to similarly target the $Val70^{Ub}$ site and the BL2 groove. **Jun13296** was nominated as an in vivo lead candidate through iterative cycles of structure-activity and structure-property relationship studies.

Literature mining has identified a similar compound recently reported by Pfizer, known as **PF-07957472**[34] (Supplementary Fig. 5). This compound closely resembles our quinoline series compounds, with a few notable differences. Specifically, the hydrophobic cyclopropyl substituent in **PF-07957472** at the methyl group position in **Jun13296** forms CH-π interactions with Tyr264 and engages with polar residues within the pocket, such as Thr301 and Asp164. The reported structure in this study, along with other solved structures[28], shows the consistent orientation of N-methyl pyrazole-quinoline aromatic rings (Supplementary Fig. 5b) (with one exception, **Jun12665**, Supplementary Fig. 5e) towards the $Val70^{Ub}$ site, which is opposite to the **PF-07957472** orientation (towards the BL2 groove).

The superposition of the PL^{pro} structure complexed to **Jun13296** with the corresponding **PF-07957472** structure (Supplementary Fig. 5d) shows that the main difference between them is the orientation of N-methyl pyrazole substituent. Meanwhile, the superposition of the PL^{pro} structure complexed to **Jun12665** with the **PF-07957472** model (Supplementary Fig. 5e) shows the same orientation of the substituents towards the BL2 groove, with **Jun12665** exhibiting the aforementioned additional hydrogen bond with the main-chain amide of Tyr268.

Jun13296 displayed more potent antiviral activity than the previously reported in vivo lead **Jun12682** in inhibiting SARS-CoV-2 variants and nirmatrelvir-resistant strains in cell culture-based assays. In vivo PK profiling showed that **Jun13296** has an oral bioavailability of 32.8% and the plasma concentration of **Jun13296** was maintained above the antiviral EC_{90} values for over 8 h with oral dosing at 50 mg/kg (Fig. 3c). In vivo assessment with a SARS-CoV-2 mouse model reveals that a 125 mg/kg BID-3 dosage of **Jun13296** provides improved mouse protection compared to **Jun12682** as demonstrated by the reduced body weight loss and mortality (Fig. 7a, b), lower lung viral load (Fig. 7d, e, i, j), and alleviated lung inflammation (Fig. 7f–h). In the experiment with a lower dosage of 75 mg/kg, **Jun13296** still rendered 90% survival protection and outperformed **Jun12682**. Intriguingly, no significant reduction in the lung viral titers was detected. Through measuring the transcriptional levels of several pro-inflammatory cytokines, we found

that the relative mRNA levels of *IL-6* and *IFN-γ*, two key cytokines associated with disease severity, were significantly reduced in the lungs of inhibitor-treated mice. We postulate that in the scenario of unaffected viral replication, the surviving mice benefited from the reduced expression of some proinflammatory cytokines (e.g., *IL-6* and *IFN-γ*), potentially through inhibiting the deubiquitinase and deISGylase activities of PL^{pro} (Fig. 4b, c). These activities mediate the deconjugation of ubiquitin or ISG15 from substrates and have been associated with modulating host immune responses through reversing the ubiquitinating and ISGylating modifications of host immune-related molecules[49–51]. In addition, free ISG15 can be secreted and play immunomodulatory functions as an extracellular cytokine[52–54]. PL^{pro} has been linked to the increasing release of ISG15 during SARS-CoV-2 infection of human macrophages[55]. Despite strong evidence supporting the immunomodulatory role of PL^{pro}, the role of its deubiquitinase and deISGylase activities, particularly during in vivo infection, has been challenging to study, due to the integrated nature of these activities with PL^{pro} polyprotein processing activity[56–59]. Reduced cytokine expression in treated mice could result from decreased viral infection or inhibition of the deubiquitinase and deISGylase activities of PL^{pro} or a combination of both. Further investigation is needed to confirm the benefit of inhibiting deubiquitinase and deISGylase activities of PL^{pro}.

Methods

Ethical statement

All procedures with live SARS-CoV-2 were performed in certified biosafety level 3 (BSL3) facilities at Oklahoma State University using biosafety protocols approved by the Institutional Biosafety Committee (IBC), which comprises scientists, biosafety and compliance experts, and members of the local community. All mouse experiments involving SARS-CoV-2 were performed within a certified animal biosafety level 3 (ABSL3) facility at Oklahoma State University. All animal studies were reviewed and approved by the Oklahoma State University Animal Care and Use Committee and met stipulations of the Guide for the Care and Use of Laboratory Animals. All research personnel received rigorous biosafety, biosecurity, and BSL3 training before participating in experiments. Personal protective equipment, including scrubs, disposable overalls, shoe covers, double-layered gloves, and powered air-purifying respirators, were used. Biosecurity measures are built in the environment through building and security systems and are reinforced through required training programs, standing meetings, and emergency exercises. The researchers involved in working with live viruses received the SARS-CoV-2 vaccines before the study was started. Finally, all researchers were medically cleared by the Oklahoma State University Occupational Health Program.

Compound synthesis and characterization

Synthesis procedures are shown in Supplementary Fig. 6-8. Compound characterization is included in the Supplementary Methods section.

Cell lines and virus

A Vero-E6 cell line, a gift from Dr. Susan Baker (Loyola University Chicago), was grown in Dulbecco's modified Eagle medium (DMEM) (Corning, 10013CM) containing 10% heat-inactivated fetal bovine serum (FBS) (Gibco, 10-438-026), 1% Pen/Strep (30-001-CI), non-essential amino acid (NEAA) (Cytiva HyClone, SH30238.01). A Vero-E6 line expressing human angiotensin-converting enzyme 2 (hACE2) and human transmembrane protease, serine 2 (hTMPRSS2) (Vero-AT), obtained through NIH-BEI Resources (NR-54970) was grown in DMEM containing 10% FBS, 1% Pen/Strep, 1× NEAA, and 10 μg/mL puromycin (InVivogen, ant-pr-1) to maintain the expression of hTMPRSS2 and hACE2. A Caco-2 line expressing hACE2 and hTMPRSS2 (Caco2-AT)[60], a gift from Dr. Mohsan Saeed (Boston University), was propagated in DMEM containing 10% FBS, 1% Pen/Strep, 1× NEAA, 1 μg/mL puromycin, and 1 μg/mL blasticidin (InVivogen, ant-bl-05).

The mouse-adapted SARS2-N501Y_{MA30} virus, a gift from Dr. Stanley Perlman (University of Iowa), was propagated once with Vero-AT cells and titrated with Vero-E6 cells. The following SARS-CoV-2 strains/isolates were obtained through BEI Resources, NIAID, NIH: Washington strain 1 (WA1) (NR-52281), recombinant SARS-CoV-2 expressing nano-luciferase reporter (icSARS-CoV-2-nLuc) (NR-54003), Omicron JN.1 variant (NR-59693), and Omicron XBB1.16 variant (NR-59442). These viruses were propagated once with Vero-AT cells to obtain large viral stocks and titrated with Vero-AT cells. A recombinant wild-type SARS-CoV-2 WA1 strain (rSARS-CoV-2) and nirmatrelvir-resistant mutants rL50F/E166V and rL50F/E166A/L167F were generated previously[14]. These viruses were full-genome sequenced using the ARTIC method[61].

Protein expression, purification and crystallization

The PL^{pro} bacterial expression plasmid, obtained from BEI Resources, NIAID, NIH (Vector pMCSG53 containing the SARS-related coronavirus 2, Wuhan-Hu-1 papain-like protease gene, NR-52897), was used to produce SARS-CoV-2 PL^{pro} following a previously described procedure with minor modifications[28]. The protein construct was expressed in *E. coli* BL21 (DE3) cultured in LB medium supplemented with ampicillin (100 μg/ml). Protein overexpression was induced by adding 1 mM isopropyl β-D-1-thiogalactopyranoside (IPTG) at an OD600 of 0.8. After 18 hours of growth at 16 °C with slow agitation, cells were pelleted by centrifugation at 7000×g, washed with PBS, and stored at -80 °C until purification.

The cell pellets were resuspended in 12.5 ml of lysis buffer (500 mM NaCl, 5% (v/v) glycerol, 50 mM HEPES pH 8.0, 20 mM imidazole, 1 mM TCEP, 1 μM ZnCl2) per liter of culture and sonicated at 120 W for 12 minutes (5 s ON, 20 s OFF). The lysate was clarified by centrifugation at 37,000×g for 90 minutes at 4 °C. Ni-NTA purification was performed according to the manufacturer's recommendations (Qiagen, Valencia, CA, USA) using the lysis buffer. Bound PL^{pro} was eluted with 20 ml of lysis buffer supplemented with 500 mM imidazole pH 7.5, followed by treatment with tobacco etch virus (TEV) protease at a 1:25 protease ratio at 4 °C overnight in dialysis buffer, and a reverse Ni-NTA purification.

After confirming His-tag cleavage by SDS-PAGE, the dialyzed protein solution was passed over a 10-mL Ni-NTA gravity column to remove His-tagged impurities. The column flowthrough was collected, analyzed by SDS-PAGE, and concentrated using a 10 kDa molecular weight cutoff Amicon Ultra-15 ultrafiltration membrane. Size exclusion chromatography was performed on a Superdex 200 Increase 10/300 GL column equilibrated with 150 mM NaCl, 50 mM Tris-HCl pH 7.5, 1 μM $ZnCl_2$, and 1 mM TCEP. Peak fractions were pooled, and the buffer was exchanged for a final buffer with a similar composition, replacing the reducing agent TCEP with either 10 mM DTT or 10 mM BME as needed. The final PL^{pro} concentration was 20 mg/ml.

A similar approach was utilized for the crystallization of PL^{pro} and six inhibitor complexes, as described previously[28]. Pure PL^{pro} protein at 20 mg/ml in 50 mM Tris-HCl pH 7.5, 150 mM NaCl, and 1 mM TCEP/10 mM DTT/10 mM BME was mixed with inhibitors at a molar ratio of 1:10 and incubated for 1 hour at 4 °C. The PL^{pro}-inhibitor complexes were clarified by high-speed centrifugation at 4 °C for 15 minutes. The sitting drop vapor diffusion method was employed using an Oryx8 robot (Douglas Instruments Ltd) in a 96-well Intelli-Plate (Art Robbins Instruments). Co-crystallizations were attempted with protein-to-well solution ratios of 1:1, 2:1, and 1:2 at 4 °C, using a focused screen based on the SARS-CoV-2 PL^{pro} PDB deposited conditions. This screen specifically included a grid prepared with 200 mM zinc acetate, 0.1 M Bis-Tris pH 5.5-6.6, and 6-20% PEG 8000. Pyramidal-shaped crystals (~ 200 μm) grew overnight, belonging to space group $I4_122$, with one copy of the complex in the asymmetric unit. Crystals selected for data collection were transferred into 1-2 μl of a cryoprotective solution consisting of crystallization buffer (without inhibitor) supplemented to a final concentration of 20% glycerol/ethylene glycol. After a few seconds, the

crystals were looped up and flash-cooled in liquid nitrogen. All crystal manipulations were conducted at 4 °C.

Data collection, structure determination, and refinement

Diffraction data were collected at 100 K for the PL^{pro} complex with **Jun12665** on beamline 12-2 at the Stanford Synchrotron Radiation Lightsource (Menlo Park, CA) at a wavelength of 0.97 Å, while data for the PL^{pro} complexes with **Jun13317, Jun13306, Jun13307, Jun13308**, and **Jun13296** were collected on beamline 17-ID-1 (AMX) at NSLS-II at Brookhaven National Laboratory (Upton, NY) at a wavelength of 0.92 Å, using Pilatus 6 M and Eiger 9 M detectors, respectively. The datasets were collected remotely, with crystal rastering performed prior to data collection to locate the best diffraction positions. Diffraction data for the complexes were collected with 200° of data per crystal and a 0.1° oscillation per image, except for the PL^{pro}-**Jun12665** complex, for which 360° was collected using a 0.2° oscillation.

For all the datasets, autoprocessed files from XDS were subsequently scaled using Aimless[62] or autoPROC from Global Phasing[63]. Initial phases for each inhibitor structure were obtained by molecular replacement using PDB 7JIT as the starting model in Phaser[64]. The inhibitor electron density was examined, and the inhibitor molecules were fitted using Coot[65]. To improve the inhibitor and protein models, iterative refinement was performed by manual model building in Coot alternating with refinement in Phenix[66]. Solvent molecules were added using 2mFo-Fc and Fo-Fc maps as guides. Statistics for diffraction data processing and the converged refinement statistics for all six datasets, along with R, Rfree, and other validation measures, are presented in Table S1. The inhibitor restraints were generated using the Grade online server[67]. PL^{pro}-inhibitor complex structures were analyzed, and figures showing the protein-inhibitor co-crystal structures were created with PyMOL (The PyMOL Molecular Graphics System, Version 1.2, Schrödinger, LLC).

Differential Scanning Fluorimetry (DSF)

The drug-binding assay was performed in the Thermo Fisher SuantStudio 5 Real-time PCR system. 4 μM of SARS-CoV-2 PL^{pro} dissolved in the reaction buffer (HEPES 50 mM, DTT 5 mM, Trion X-100 0.01%, pH 7.2) was mixed with different concentrations of compounds. After 30 min of 30 °C incubation, 1x final concentration of SYPRO orange (Invitrogen, #S6650) was added to the mixture. The fluorescence was monitored with temperature rising from 25 °C to 95 °C at the increment of 0.05 °C/s. The melting temperature (T_m) of each sample was obtained by the mid-log of the transition phase from the native to denatured protein using the Boltzmann model in Protein Thermal Shift Software v1.3.

Enzymatic assays

The enzymatic assay of SARS-CoV-2 PL^{pro} digesting Ub-AMC (UBPBIO, #M3010) was performed by mixing 50 nM of SARS-CoV-2 PL^{pro} with various concentrations of compounds in the reaction buffer (HEPES 50 mM, DTT 5 mM, Triton X-100 0.01%, pH 7.2). After the incubation of 10 min at 30 °C, Ub-AMC was added to the reaction to a final concentration of 2.5 μM. The fluorescence was monitored every 71 s with the excitation of 360/40 nm and emission of 460/40 nm for 3 h at 30 °C, using a Cytation 5 plate reader. The K_i was determined by plotting the first 1 h of initial velocity against the compound concentrations using the Morrison equation for tight binding $(Y = V_O*(1 - ((((E_t + X + (K_i*(1 + (S/K_m))))) - (((E_t + X + (K_i*(1 + (S/K_m))))^2) - 4*E_t*X)^{0.5}))/(2*E_t)))$, X = inhibitor concentration; Y = enzyme velocity; E_t = enzyme concentration; V_O = enzyme velocity in the absence of inhibitor). The enzymatic assay of SARS-CoV-2 PL^{pro} digesting ISG15-AMC (R&D, #UL-553) was performed similarly with the changes in protein and substrate concentrations. The final concentration of SARS-CoV-2 PL^{pro} was 2 nM and of ISG15-AMC was 0.5 μM in the ISG15 assays. All reported data were the average of 2 replicates with standard error with a 95% confidence interval calculated as SE = (upper limit − lower limit)/3.92.

The counter-screening assays with USP14 (ProSci, 91-171) and USP7(Sino Biological, #11681-H20B) were performed in the USP reaction buffer (HEPES 50 mM, pH 7.2, BSA 0.1 mg/mL, Triton X-100 0.01%, DTT 5 mM, Glycerol 5%). Compounds were incubated with 40 nM of USP7 and 800 nM of USP14 respectively for 10 min at 30 °C. 5 μM of Ub-AMC was added to initiate the reaction. The fluorescence was monitored, and initial velocities of each group were taken to compare with the DMSO-treated group. Values reported were performed in 2 replicates and error bars represent standard deviation.

Cell-Based FlipGFP-PL^{pro} assay

The FlipGFP-PL^{pro} assay was performed following the published procedures[28,31,32]. Briefly, the reporter plasmid pcDNA3-TEV-flipGFP-T2A-mCherry was obtained from Addgene (catalog no.124429). SARS-CoV-2 PL^{pro} cleavage site LRGG↓APTK was introduced into pcDNA3-FlipGFP-T2AmCherry via overlapping PCRs to generate a fragment with SacI and HindIII sites at the ends. SARS-CoV-2 PL^{pro} expression plasmid pcDNA3.1 SARS2 PL^{pro} was ordered from Genscript (Piscataway, NJ) with codon optimization. For transfection, HEK293T cells were seeded in 96-well Greiner plate (catalog no. 655090) and grown overnight to achieve 70–80% confluency. A total of 9 μL of Opti-MEM, 0.1 μL of 500 ng/μL pcDNA3-flipGFP-T2A-mCherry plasmid, 0.1 μL of 500 ng/μL protease expression plasmid pcDNA3.1, and 0.3 μL of transIT-293 (Mirus) were added to each well of a 96-well plate. Three hours after transfection in a cell culture incubator (humidified, 5% CO_2/95% air, 37 °C), 1 μL of testing compound was added to each well at 100-fold dilution. Images were acquired 48 h after transfection with a Celigo Image Cytometer (Nexcelom) and were analyzed with Gen5 3.10 software (Biotek). SARS-CoV-2 PL^{pro} protease activity was calculated by the ratio of GFP signal sum intensity over the mCherry signal sum intensity. The FlipGFP-PL^{pro} assay IC_{50} value was calculated by plotting the GFP/mCherry signal over the applied compound concentration with a four-parameter dose-response function in Prism 8. The mCherry signal alone was utilized to determine the compound cytotoxicity.

Enzymatic counter screenings against host proteases

The enzymatic assay of human ubiquitinase in digesting Ub-AMC substrate (UBPBIO, M3010) was performed in a 384-well plate. The ubiquitinases were dissolved in the reaction buffer (50 mM HEPES, 0.1 mg/mL BSA, 0.01% Triton X-100, 5 mM DTT, and 5% glycerol in 50 μL) to the final concentrations: 1 nM USP2 (R&D systems, E504), 20 nM USP7 (Sino Biological, 11681-H20B), 20 nM USP8 (Boston Biochem. E-520-025), 500 nM USP14 (ProSci, 91-171), 1 nM USP15 (R&D systems, E594), 20 nM USP30 (R&D systems, E582), and 1 nM UCH-L1 (R&D systems, 6007-CY). Then, 1 μL of **Jun13296** with various concentrations or DMSO control was added to the PL^{pro} protein solution. The PL^{pro} protein with **Jun13296** was mixed by shaking and incubating at 30 °C for 30 min. The enzymatic reaction was initiated by adding 1 μL Ub-AMC substrate (UBPBIO, M3010) to a final concentration of 2 μM. The fluorescent signal was monitored at excitation of 360 nm and emission of 460 nm. The first 500 s of the initial velocity of each reaction was calculated by GraphPad Prism 8.0 and was compared with the DMSO-treated group to determine the inhibition of **Jun13296**.

The enzymatic assays of Cathepsin B and K were performed as previously described[68]. 100 μl of cathepsin B or K was dissolved in the reaction buffer (20 mM sodium acetate, 1 mM EDTA, 5 mM DTT). The final concentration of the enzymes were 1.5 nM of cathepsin B and 100 nM of cathepsin K. The enzyme solutions were incubated at 30 °C for 30 minfor activation, followed by the addition and incubation of **Jun13296**. The reaction was initiated by the addition of the substrate Z-FR-AMC to a final concentration of 5 μM.

Calpain 1 (Sigma, C6108) were dissolved in the reaction buffer (50 mM HEPES, 50 mM NaCl, 10 mM DTT, and 5 mM $CaCl_2$) in 100 μL. The final concentration of calpain 1 was 0.01 μg/mL. Then, 1 μL of

Jun13296 in various concentrations or DMSO control was added to the PL^{pro} protein solution. The PL^{pro} protein with **Jun13296** was mixed by shaking and incubating at 30 °C for 30 min. The enzymatic reaction was initiated by the addition of 1 μL of 4 mM N-succinyl-Leu-Leu-Val-Tyr-7-amino-4-methylcoumarin (Sigma, S6510) substrate.

Caspase-3 (BioVision, 1083) was dissolved in the reaction buffer (20 mM sodium acetate, 1 mM EDTA, 5 mM DTT) in 100 μL. The final concentration of Caspase-3 was 0.01 unit/μL. Then, 1 μL of **Jun13296** with various concentrations or DMSO control was added to the Caspase-3 solution. The Caspase-3 with **Jun13296** was mixed by shaking and incubating at 30 °C for 30 min. The enzymatic reaction was initiated by the addition of 1 μL of 2 mM Ac-DEAD-AMC substrate.

Trypsin (Sigma, T6763) was dissolved in the reaction buffer (50 mM HEPES, 50 mM NaCl, 10 mM DTT) in 100 μL. The final concentration of trypsin was 20 μg/mL. Then, 1 μL of **Jun13296** with various concentrations or DMSO control was added to the trypsin solution. The trypsin with **Jun13296** was mixed by shaking and incubating at 30 °C for 30 min. The enzymatic reaction was initiated by the addition of 1 μL of 2 mM Bz-R-AMC (Bachem, 4002540.0050) substrate. The fluorescent signal was monitored at excitation of 360 nm and emission of 460 nm. The first 500 seconds of the initial velocity of each reaction was calculated by GraphPad Prism 8.0 and was compared with the DMSO-treated group to determine the inhibition of **Jun13296**.

Antiviral assays with live SARS-CoV-2

A SARS-CoV-2 reporter virus assay and an antiviral plaque assay were employed for antiviral effect evaluation. The reporter virus assay was performed as described previously[30]. Briefly, Caco2-AT cells at a density of 1.5×10^4 cells/well were batch inoculated with icSARS-CoV-2-nLuc at a MOI of 0.2 and then added to 96-well plates with 50 μL per well of DMEM containing 4% FBS and 2 μM CP-100356. To prepare compound solutions, the test compounds and positive control (**Jun12682**) were 3-fold serially diluted in DMEM, starting at 30 μM final concentration for the testing compounds. After dilution, 50 μL diluted compound solution was transferred and mixed (1:1 volume ratio) with the cell-virus mixture pre-seeded in 96-well plates. Cells were incubated for 24 h at 37 °C with 5% CO_2 and then subjected to a Nano-Glo Luciferase assay (Promega, G9243) on a Promega GloMax Discover microplate reader (Promega, GM3000) following the manufacturer's instructions. The raw data were analyzed with Prism 10 using the non-linear regression curve fit method.

The antiviral plaque assay was performed similarly as we described previously[28]. Briefly, Vero-AT cells (3.0×10^5 cells/well) were seeded in 12-well plates a day before viral infection. The PL^{pro} inhibitors dissolved in DMSO were serially diluted in DMEM with 3-fold dilutions between test concentrations, starting at 10 μM final concentration for PL^{pro} inhibitors or 1 μM final concentration for nirmatrelvir. Cells in 12-well plates were infected with approximately 20 plaque-forming units (PFU) per well for 1 h. After incubation, the inoculum was removed and 1 mL 1X DMEM-1.2% Avicel (FMC polymers) mixture containing serially-diluted compound and 2 μM CP-100356 was added to each well. After 48 h of incubation at 37 °C, the DMEM-Avicel mixture was removed and the cells were stained using 0.1% crystal violet solution. Plates were photographed and measured for the area of cells affected by infection using ImageJ.

Mouse experiments

Nine to twelve-week-old female BALB/c mice (Strain #: 000651) were procured from the Jackson Laboratory and acclimated for a week before viral inoculation in standard vivarium conditions of dark/light cycle, ambient temperature, and humidity. The animal sex was not considered in the study design as both sexes of mice are susceptible to SARS2-$N501Y_{MA30}$ infection. Mice were randomly assigned to different groups, with numbers per group sufficient to obtain statistical significance. For virus inoculation, mice were briefly anesthetized with isoflurane and inoculated intranasally (i.n.) with 6000 PFU of SARS2-$N501Y_{MA30}$ in a total volume of 50 μL DMEM. PL^{pro} inhibitors were dissolved in 0.5% methylcellulose solution containing 2% Tween-80 and administered via oral gavage using 20 G/30 mm plastic feeding tubes (Instech, FTP203050). Oral treatment with PL^{pro} inhibitors or vehicle started one-hour post-virus inoculation, following a twice-daily, 10 h–14 h interval administration for 3 days. Mouse body weight and health were monitored daily. Mice losing 20% of body weight were humanely euthanized (predefined endpoint). The weight loss and mortality results were analyzed with Prism 10. A group of 5 mice for each treatment group were euthanized at 2- and 4-day post-infection (DPI) for necropsy. The left lungs were collected in pre-filled bead tubes (Fisher Scientific, 15-340-153) filled with 1 mL DMEM for viral load determination. For histopathological analyses, the remaining portion of the lungs was infused with 1 mL zinc-buffered formalin solution (Fisher Scientific, STLBFZ1), followed by removal and fixation with 30 mL zinc-buffered formalin solution for at least two days before removal from ABSL3 per an approved IBC protocol.

Lung viral titer determination by plaque assay

The left lung tissues were homogenized in pre-filled bead tubes using an automated homogenizer (Fisherbrand™, 15-340-164), followed by centrifugation ($500 \times g$ for 5 min). The clarified tissue homogenate supernatants were aliquoted and stored at −80 °C or subjected to a standard plaque assay with Vero-AT cells. The supernatants were serially diluted in DMEM and inoculated onto Vero-AT cells in six-well plates and maintained at 37 °C in 5% CO_2 for 1 h with gentle rocking every 15 min. After removing the inoculum, plates were overlaid with 1.2% agarose (Fisherbrand, BP160-500)-1X DMEM mix containing 2% FBS. After 2 days, overlays were removed, and plaques were visualized by staining with 0.1% crystal violet. Viral titers were quantified as PFU per mL tissue homogenate.

Lung histology and immunohistochemistry (IHC)

Fixed tissues were trimmed and processed using a Sakura Tissue-Tek VIP® 6 AI tissue processor (Sakura Finetek USA, Inc. 1750 214th St, Torrence CA, 90501) on a delayed short cycle program and embedded in paraffin (Leica Surgipath Paraplast Infiltration and Embedding Medium; Leica Biosystems). Paraffin blocks were cut into 4 μm-thick sections and mounted on VistaVision HistoBond adhesive glass slides from VWR (Radnor, PA). Hematoxylin and eosin (H&E) staining was performed following standard operating procedures with the Sakura Finetek DRS601 (Sakura Finetek USA, Inc., 1750 West 214th Street, Torrance, CA 90501). For IHC, slides were rehydrated with water, following HIER (Heat Induced Epitope Retrieval) performed at 95 °C for 20 min in Citrate Unmasking solution (H-3300, Vector Laboratories, Newark, CA). SARS-CoV-2 Nucleocapsid antibody [HL448] (Genetex, GTX635686) was diluted 1:5000 in TBS-Tween 20 buffer with 10% normal goat serum and slides were incubated for 1 h at room temperature (RT). Slides were washed in TBS-Tween 20 buffer and then quenched of endogenous peroxidase using 0.3% H_2O_2 for 10 min. Slides were washed and detection was carried out using VECTASTAIN® Elite® ABC-HRP Kit, Peroxidase (Rabbit IgG) (Vector Laboratories, PK-6101) per the manufacturer's instructions. Hematoxylin diluted 1:10 was used as a counterstain. Stained tissue sections were evaluated by a board-certified veterinary pathologist for three parameters: presence of edema or hyaline membranes, perivascular lymphoid inflammation, and interstitial inflammation. Edema or hyaline membranes were evaluated using a distribution-based ordinal scoring on a scale of 0 to 5 with 0, none; 1, <5%; 2, 6–25%; 3, 26–50%; 4, 51–75%; and 5, >75% of tissue affected. Perivascular lymphoid inflammation and interstitial pneumonia were evaluated using a severity-based ordinal scoring system on a scale of zero to four: 0 (absent), 1 (minimal), 2 (mild), 3 (moderate), and 4 (severe). An accumulative score is calculated by summing the ordinal scores of the three parameters. IHC was scored using a distribution-based ordinal scoring of 0 to 5 with 0, none; 1, <5%; 2, 6–25%; 3, 26–50%; 4, 51–75%; and 5, >75% of tissue affected.

Table 1 | Primers used in the qPCR

Gene	Forward (5′- > 3′)	Reverse (5′- > 3′)
SARS-CoV-2 N gene	AAGCTGGACTTCCCTATGGTG	CGATTGCAGCATTGTTAGCAGG
Mouse *IL-6*	GCTACCAAACTGGATATAATCAGGA	CCAGGTAGCTATGGTACTCCAGAA
Mouse *IL-1β*	TGGACCTTCCAGGATGAGGACA	GTTCATCTCGGAGCCTGTAGTG
Mouse *CXCL10*	GCTTCCCTATGGCCCTCATT	GCCGTCATTTTCTGCCTCAT
Mouse *IFN-γ*	CAGCAACAGCAAGGCGAAAAAGG	TTTCCGCTTCCTGAGGCTGGAT
Mouse *18S rRNA*	TCGGAACTGAGGCCATGATT	TTTCGCTCTGGTCCGTCTTG

RNA extraction and Real-time PCR quantification

Total RNA was extracted from the lung homogenate supernatants using TRIzol (Invitrogen, 15596018). A total of 1000 ng RNA was used for cDNA synthesis using the RT² HT First Strand Kit (QIAGEN, 330411), which contains a component to eliminate genomic DNA contamination. Quantitative PCR was performed with specific primers (Table 1) using PowerUp SYBR Green Master mix (Fisher, A25918) on QuantStudio 6 Pro (ThermoFisher, A43160). Cycle threshold values were normalized to 18S rRNA levels by using the $2^{-\Delta Ct}$ method.

Reporting summary

Further information on research design is available in the Nature Portfolio Reporting Summary linked to this article.

Data availability

Crystal structures generated during the current study are available in the Protein Data Bank (PDB) under accession codes 9DO3 (PL^{pro} bound to **Jun13317**), 9DNV (PL^{pro} bound to **Jun13308**), 9DO1 (PL^{pro} bound to **Jun13307**), 9DOI (PL^{pro} bound to **Jun13306**). 9DNU (PL^{pro} bound to **Jun13296**) and 9DO5 (PL^{pro} bound to **Jun12665**). The mouse-adapted SARS2-N501YMA30 virus was obtained from Dr. Stanley Perlman at the University of Iowa and the availability of this virus is restricted under a materials transfer agreement (MTA) with the University of Iowa. The request for this virus should be directed to Dr. Stanley Perlman. The recombinant SARS-CoV-2 nsp5 mutant viruses are available upon request by contacting Xufang Deng through an MTA with Oklahoma State University. Requests will be processed within 8 weeks, and if approved, arrangements will be made for materials transfer. The following SARS-CoV-2 strains/isolates were obtained through and available at BEI Resources (https://www.beiresources.org/), NIAID, NIH: Washington strain 1 (WA1) (cat# NR-52281), recombinant SARS-CoV-2 expressing nano-luciferase reporter (icSARS-CoV-2-nLuc) (cat# NR-54003), Omicron JN.1 variant (cat# NR-59693), and Omicron XBB1.16 variant (cat# NR-59442). These viruses may be further distributed to other entities for any legitimate purpose required to rapidly prevent, detect, prepare for, and respond to, the spread or transmission of SARS-CoV-2, as described in an Emergency Use Simple Letter Agreement (EUSLA) Article 1. An MTA is needed for further distribution and must be reported to BEI (contact@beiresources.org). Source data are provided with this paper as Source Data file. Source data are provided with this paper.

References

1. Li, G., Hilgenfeld, R., Whitley, R. & De Clercq, E. Therapeutic strategies for COVID-19: progress and lessons learned. *Nat. Rev. Drug Discov.* **22**, 449–475 (2023).
2. Shoichet, B. K. & Craik, C. S. Preparing for the next pandemic. *Science* **382**, 649–650 (2023).
3. Boby, M. L. et al. Open science discovery of potent noncovalent SARS-CoV-2 main protease inhibitors. *Science* **382**, eabo7201 (2023).
4. Karim, M., Lo, C. W. & Einav, S. Preparing for the next viral threat with broad-spectrum antivirals. *J. Clin. Investig.* **133**, e170236 (2023).
5. Radoshitzky, S. R. et al. Expanded profiling of Remdesivir as a broad-spectrum antiviral and low potential for interaction with other medications in vitro. *Sci. Rep.* **13**, 3131 (2023).
6. Malin, J. J., Suárez, I., Priesner, V., Fätkenheuer, G. & Rybniker, J. Remdesivir against COVID-19 and Other Viral Diseases. *Clin. Microbiol. Rev.* **34**, e00162–20 (2020).
7. Kabinger, F. et al. Mechanism of molnupiravir-induced SARS-CoV-2 mutagenesis. *Nat. Struct. Mol. Biol.* **28**, 740–746 (2021).
8. Joyce, R. P., Hu, V. W. & Wang, J. The history, mechanism, and perspectives of nirmatrelvir (PF-07321332): an orally bioavailable main protease inhibitor used in combination with ritonavir to reduce COVID-19-related hospitalizations. *Med. Chem. Res.* **31**, 1637–1646 (2022).
9. Owen, D. R. et al. An oral SARS-CoV-2 M(pro) inhibitor clinical candidate for the treatment of COVID-19. *Science* **374**, 1586–1593 (2021).
10. Tan, B., Joyce, R., Tan, H., Hu, Y. & Wang, J. SARS-CoV-2 main protease drug design, assay development, and drug resistance studies. *Acc. Chem. Res.* **56**, 157–168 (2023).
11. Unoh, Y. et al. Discovery of S-217622, a Noncovalent Oral SARS-CoV-2 3CL protease inhibitor clinical candidate for treating COVID-19. *J. Med. Chem.* **65**, 6499–6512 (2022).
12. Allerton, C. M. N. et al. A second-generation oral SARS-CoV-2 main protease inhibitor clinical candidate for the treatment of COVID-19. *J. Med. Chem.* **67**, 13550–13571 (2024).
13. Shurtleff, V. W. et al. Invention of MK-7845, a SARS-CoV-2 3CL protease inhibitor employing a novel difluorinated glutamine mimic. *J. Med. Chem.* **67**, 3935–3958 (2024).
14. Hu, Y. et al. Naturally occurring mutations of SARS-CoV-2 main protease confer drug resistance to nirmatrelvir. *ACS Cent. Sci.* **9**, 1658–1669 (2023).
15. Sacco, M. D. et al. The P132H mutation in the main protease of Omicron SARS-CoV-2 decreases thermal stability without compromising catalysis or small-molecule drug inhibition. *Cell Res.* **32**, 498–500 (2022).
16. Iketani, S. et al. Multiple pathways for SARS-CoV-2 resistance to nirmatrelvir. *Nature* **613**, 558–564 (2022).
17. Zhou, Y. et al. Nirmatrelvir-resistant SARS-CoV-2 variants with high fitness in an infectious cell culture system. *Sci. Adv.* **8**, eadd7197 (2022).
18. Jochmans, D. et al. The Substitutions L50F, E166A, and L167F in SARS-CoV-2 3CLpro Are Selected by a protease inhibitor in vitro and confer resistance to Nirmatrelvir. *mBio*, **14**, e0281522 (2023).
19. Kiso, M. et al. In vitro and in vivo characterization of SARS-CoV-2 strains resistant to nirmatrelvir. *Nat. Commun.* **14**, 3952 (2023).
20. Abdelnabi, R. et al. Nirmatrelvir-resistant SARS-CoV-2 is efficiently transmitted in female Syrian hamsters and retains partial susceptibility to treatment. *Nat. Commun.* **14**, 2124 (2023).
21. Zuckerman, N. S., Bucris, E., Keidar-Friedman, D., Amsalem, M. & Brosh-Nissimov, T. Nirmatrelvir resistance - de novo E166V/L50V mutations in an immunocompromised patient treated with prolonged nirmatrelvir/ritonavir monotherapy leading to clinical and virological treatment failure - a case report. *Clin. Infect. Dis.* **78**, 352–355 (2023).
22. Rut, W. et al. Activity profiling and crystal structures of inhibitor-bound SARS-CoV-2 papain-like protease: A framework for anti-COVID-19 drug design. *Sci. Adv.* **6**, eabd4596 (2020).
23. Shin, D. et al. Papain-like protease regulates SARS-CoV-2 viral spread and innate immunity. *Nature* **587**, 657–662 (2020).
24. Wydorski, P. M. et al. Dual domain recognition determines SARS-CoV-2 PLpro selectivity for human ISG15 and K48-linked di-ubiquitin. *Nat. Commun.* **14**, 2366 (2023).

25. Tan, H., Hu, Y., Jadhav, P., Tan, B. & Wang, J. Progress and challenges in targeting the SARS-CoV-2 Papain-like protease. *J. Med. Chem.* **65**, 7561–7580 (2022).
26. Sanders, B. C. et al. Potent and selective covalent inhibition of the papain-like protease from SARS-CoV-2. *Nat. Commun.* **14**, 1733 (2023).
27. Ghosh, A. K., Mishevich, J. L., Mesecar, A. & Mitsuya, H. Recent drug development and medicinal chemistry approaches for the treatment of SARS-CoV-2 infection and COVID-19. *ChemMedChem* **17**, e202200440 (2022).
28. Tan, B. et al. Design of a SARS-CoV-2 papain-like protease inhibitor with antiviral efficacy in a mouse model. *Science* **383**, 1434–1440 (2024).
29. Shen, Z. et al. Design of SARS-CoV-2 PLpro inhibitors for COVID-19 antiviral therapy leveraging binding cooperativity. *J. Med. Chem.* **65**, 2940–2955 (2022).
30. Jadhav, P. et al. Structure-based design of SARS-CoV-2 papain-like protease inhibitors. *Eur. J. Med. Chem.* **264**, 116011 (2024).
31. Tan, H., Hu, Y. & Wang, J. FlipGFP protease assay for evaluating in vitro inhibitory activity against SARS-CoV-2 M(pro) and PL(pro). *STAR Protoc.* **4**, 102323 (2023).
32. Ma, C. et al. Discovery of SARS-CoV-2 papain-like protease inhibitors through a combination of high-throughput screening and a FlipGFP-based reporter assay. *ACS Cent. Sci.* **7**, 1245–1260 (2021).
33. Klemm, T. et al. Mechanism and inhibition of the papain-like protease, PLpro, of SARS-CoV-2. *EMBO J.* **39**, e106275 (2020).
34. Garnsey, M. R. et al. Discovery of SARS-CoV-2 papain-like protease (PL(pro)) inhibitors with efficacy in a murine infection model. *Sci. Adv.* **10**, eado4288 (2024).
35. Zhang, L. et al. Viral anti-inflammatory serpin reduces immunocoagulopathic pathology in SARS-CoV-2 mouse models of infection. *EMBO Mol. Med.* **15**, e17376 (2023).
36. Wang, G. et al. Universal subunit vaccine protects against multiple SARS-CoV-2 variants and SARS-CoV. *NPJ Vaccines* **9**, 133 (2024).
37. Fumagalli, V. et al. Antibody-independent protection against heterologous SARS-CoV-2 challenge conferred by prior infection or vaccination. *Nat. Immunol.* **25**, 633–643 (2024).
38. Fumagalli, V. et al. Nirmatrelvir treatment of SARS-CoV-2-infected mice blunts antiviral adaptive immune responses. *EMBO Mol. Med.* **15**, e17580 (2023).
39. Moore, J. B. & June, C. H. Cytokine release syndrome in severe COVID-19. *Science* **368**, 473–474 (2020).
40. Coomes, E. A. & Haghbayan, H. Interleukin-6 in Covid-19: A systematic review and meta-analysis. *Rev. Med. Virol.* **30**, 1–9 (2020).
41. Gordon, A. C. et al. Interleukin-6 receptor antagonists in critically Ill patients with Covid-19. *N. Engl. J. Med.* **384**, 1491–1502 (2021).
42. Jones, S. A. & Hunter, C. A. Is IL-6 a key cytokine target for therapy in COVID-19? *Nat. Rev. Immunol.* **21**, 337–339 (2021).
43. Shankar-Hari, M. et al. Association between administration of IL-6 antagonists and mortality among patients hospitalized for COVID-19: a meta-analysis. *JAMA* **326**, 499–518 (2021).
44. Chen, L. Y. C., Hoiland, R. L., Stukas, S., Wellington, C. L. & Sekhon, M. S. Confronting the controversy: interleukin-6 and the COVID-19 cytokine storm syndrome. *Eur. Respir. J.* **56**, 2003006 (2020).
45. Todorović-Raković, N. & Whitfield, J. R. Between immunomodulation and immunotolerance: the role of IFNγ in SARS-CoV-2 disease. *Cytokine* **146**, 155637 (2021).
46. Karki, R. et al. Synergism of TNF-α and IFN-γ triggers inflammatory cell death, tissue damage, and mortality in SARS-CoV-2 infection and cytokine shock syndromes. *Cell* **184**, 149–168.e117 (2021).
47. Krishna, B. A. et al. Spontaneous, persistent, T cell-dependent IFN-γ release in patients who progress to Long Covid. *Sci. Adv.* **10**, eadi9379 (2024).
48. Li, C. et al. Comparative single-cell analysis reveals IFN-γ as a driver of respiratory sequelae after acute COVID-19. *Sci. Transl. Med.* **16**, eadn0136 (2024).
49. Mielech, A. M., Chen, Y., Mesecar, A. D. & Baker, S. C. Nidovirus papain-like proteases: multifunctional enzymes with protease, deubiquitinating and deISGylating activities. *Virus Res.* **194**, 184–190 (2014).
50. Báez-Santos, Y. M., John, S. E. S. & Mesecar, A. D. The SARS-coronavirus papain-like protease: structure, function and inhibition by designed antiviral compounds. *Antiviral Res.* **115**, 21–38 (2015).
51. Xiong, Y. et al. The substrate selectivity of papain-like proteases from human-infecting coronaviruses correlates with innate immune suppression. *Sci. Signal.* **16**, eade1985 (2023).
52. Swaim, C. D., Scott, A. F., Canadeo, L. A. & Huibregtse, J. M. Extracellular ISG15 signals cytokine secretion through the LFA-1 integrin receptor. *Mol. Cell* **68**, 581–590.e585 (2017).
53. Perng, Y. C. & Lenschow, D. J. ISG15 in antiviral immunity and beyond. *Nat. Rev. Microbiol.* **16**, 423–439 (2018).
54. Sarkar, L., Liu, G. & Gack, M. U. ISG15: its roles in SARS-CoV-2 and other viral infections. *Trends Microbiol.* **31**, 1262–1275 (2023).
55. Munnur, D. et al. Altered ISGylation drives aberrant macrophage-dependent immune responses during SARS-CoV-2 infection. *Nat. Immunol.* **22**, 1416–1427 (2021).
56. Clasman, J. R., Everett, R. K., Srinivasan, K. & Mesecar, A. D. Decoupling deISGylating and deubiquitinating activities of the MERS virus papain-like protease. *Antiviral Res.* **174**, 104661 (2020).
57. Deng, X. et al. Structure-guided mutagenesis alters deubiquitinating activity and attenuates pathogenesis of a murine coronavirus. *J. Virol.* **94**, e01734-19 (2020).
58. Myeni, S. K. et al. Engineering potent live attenuated coronavirus vaccines by targeted inactivation of the immune evasive viral deubiquitinase. *Nat. Commun.* **14**, 1141 (2023).
59. van Huizen, M. et al. Deubiquitinating activity of SARS-CoV-2 papain-like protease does not influence virus replication or innate immune responses in vivo. *PLoS Pathog.* **20**, e1012100 (2024).
60. Chen, D. Y. et al. Cell culture systems for isolation of SARS-CoV-2 clinical isolates and generation of recombinant virus. *iScience* **26**, 106634 (2023).
61. Deng, X. et al. Breakthrough infections with multiple lineages of SARS-CoV-2 variants reveals continued risk of severe disease in immunosuppressed patients. *Viruses* **13**, 1743 (2021).
62. Evans, P. R. & Murshudov, G. N. How good are my data and what is the resolution? *Acta. Crystallogr. D Biol. Crystallogr.* **69**, 1204–1214 (2013).
63. Vonrhein, C. et al. Data processing and analysis with the autoPROC toolbox. *Acta. Crystallogr. D Biol. Crystallogr.* **67**, 293–302 (2011).
64. McCoy, A. J. et al. Phaser crystallographic software. *J. Appl. Crystallogr.* **40**, 658–674 (2007).
65. Emsley, P. & Cowtan, K. Coot: model-building tools for molecular graphics. *Acta. Crystallogr. D Biol. Crystallogr.* **60**, 2126–2132 (2004).
66. Afonine, P. V. et al. Towards automated crystallographic structure refinement with phenix.refine. *Acta. Crystallogr. D Biol. Crystallogr.* **68**, 352–367 (2012).
67. Smart, O. S. et al. Grade2 version 1.6.0. Cambridge, United Kingdom: Global Phasing Ltd. (2021).
68. Ma, C. et al. Discovery of Di- and Trihaloacetamides as Covalent SARS-CoV-2 main protease inhibitors with high target specificity. *J. Am. Chem. Soc.* **143**, 20697–20709 (2021).

Acknowledgements

We thank Shannon Cowan and Caden Miller at the Immunopathology Core of the Oklahoma Center for Respiratory and Infectious Diseases (OCRID) for their technical assistance. J.W. is funded by National Institutes of Health grants R01AI158775 and Rutgers HealthAdvance funding. Research reported in this publication was supported by the National Heart, Lung, And Blood Institute of the National Institutes of Health under Award Number U01HL150852. The content is solely the responsibility of the authors and does not necessarily represent the official views of the National Institutes of Health. E.A. is funded by National

Institutes of Health grant U19AI171110; X.D. is funded by National Institutes of Health grant R01AI158775. Research reported in this publication was made possible in part by the services of the Immunopathology Core, part of the OCRID which is supported by the NIH COBRE grant under award number P30GM149368.

Author contributions

J.W., X.D., E.A., and F.X.R. conceived and supervised the research and designed the experiments; J.W., P.J., and B.T. designed the inhibitors; P.J. and B.T. performed chemical syntheses, separation, purification, and structural characterizations; A.A. and F.X.R. performed gene expression, protein purification, crystallization, and diffraction data collection; A.A., and F.X.R., and E.A. determined and analyzed the crystal structures; B.T., H.T., and K.L. performed enzymatic inhibition assays, DSF assays, and cellular cytotoxicity assays; X.L. performed in vitro cellular antiviral assays and in vivo mouse model studies; A.F. performed the histopathology and immunohistochemistry (IHC) assessment; X.C. performed the mouse tissue analysis and assisted in the in vivo antiviral studies; J.W., P.J., B.T., X.L., A.A., A.F., X.C., F.X.R., X.D., and E.A. analyzed and discussed the data with the assistance of H.T., and K.L.; and J.W., A.A., F.X.R., E.A., and X.D. wrote the manuscript with the assistance of B.T., X.L., P.J., H.T., K.L., and A.F.

Competing interests

Rutgers, the State University of New Jersey, has applied for a patent US2024382494A1 covering the PL^{pro} inhibitors reported in this study and related compounds, which has been published and is pending. J.W. is listed as an inventor. The remaining authors declare no competing interests.

Additional information

Supplementary information The online version contains supplementary material available at https://doi.org/10.1038/s41467-025-56902-x.

Correspondence and requests for materials should be addressed to Francesc Xavier Ruiz, Eddy Arnold, Xufang Deng or Jun Wang.

Peer review information *Nature Communications* thanks Chamandi Dampalla, and the other, anonymousreviewer(s) for their contribution to the peer review of this work. A peer review file is available.